

# Comparison of $CO_2$ from NOAA Carbon Tracker reanalysis model and satellites over Africa

Anteneh Getachew Mengistu<sup>1</sup> and Gizaw Mengistu Tsidu<sup>1,2</sup>

<sup>1</sup>Addis Ababa University, Addis Ababa, Ethiopia

<sup>2</sup>Botswana International University of Science and Technology, Palapye, Botswana

**Correspondence:** Anteneh G (antenehgetachew7@gmail.com)

**Abstract.** The scarcity of ground-based observations, poor spatial and temporal resolution of satellite observations necessitate the use of data generated from models to assess spatio-temporal variations of atmospheric  $CO_2$  concentrations in a near continuous manner in a global and regional scale. Africa is one of the most data scarce region as satellite observation at the equator is limited by cloud cover and there are very limited number of ground based measurements. As a result, use of simulations from models are mandatory to fill this data gap. However, the first step before the use of data from models requires assessment of model skill in simulating limited existing observations reasonably well. Even though, the NOAA Carbon Tracker model is evaluated using TCCON and satellite observations at a global level, its performance should be assessed at a regional scale, specifically in a regions like Africa with a highly varying climatic responses and a growing number of local sources. In this study, NOAA CT2016  $XCO_2$  is compared with the GOSAT observation over Africa using five years data covering the period from May 2009 to April 2014. In addition, NOAA CT16NRT17  $XCO_2$  is compared with OCO-2 observation over Africa using two years data covering the period from January 2015 to December 2016. The analysis shows that the  $XCO_2$  simulated from CT2016 is lower than GOSAT retrievals by 0.28 ppm whereas CT16NRT17  $XCO_2$  is higher than OCO-2 retrievals by 0.34 ppm on African landmass on average, which are within the mean  $XCO_2$  posterior errors of 0.91 and 0.55 ppm associated with the GOSAT and OCO-2  $XCO_2$  retrievals respectively. The mean correlations of 0.83 and 0.60, regional precisions of 2.30 and 2.57 ppm, and the relative accuracies of 1.05 and 1.21 ppm are found between the model and the two data sets implying the existence of reasonably good agreement between CT and the two satellites over Africa's land region given that very limited number of in-situ observations over the region is assimilated in the model. These differences, however, exhibit spatial and seasonal scale variations. Moreover, the model shows some differences with the observations at extreme ends of  $XCO_2$  distribution. For example, the quantile probability of detection ranges from 0.42 to 0.99 and quantile critical success index ranges from 0.37 to 0.93 over the continent when the analysis includes data above the 90<sup>th</sup> and 5<sup>th</sup> percentiles respectively (see main text for definitions). This shows that the model disagrees with observations on 58% of  $XCO_2$  with values higher than 90<sup>th</sup> percentile. This discrepancy increases to approximately 80% at 95<sup>th</sup> percentile indicating the agreement between CT and the satellites deteriorates towards the high extreme ends of the  $XCO_2$  distribution. Spatially, OCO-2  $XCO_2$  are lower than that of CT16NRT17 by upto 3 ppm over some regions in North Africa (e.g., Egypt, Libya and Mali ) whereas it exceeds CT16NRT17  $XCO_2$  by 2 ppm over Equatorial Africa ( $10^{\circ}S - 10^{\circ}N$ ). CT2016 shows high spatial mean of seasonal mean RMSD of 1.91 ppm during DJF with respect to GOSAT while CT16NRT17 shows 1.75 ppm during

MAM with respect to OCO-2. On the other hand, low RMSD of 1.00 and 1.07 ppm during SON in the model  $XCO_2$  with respect to GOSAT and OCO-2 are determined respectively indicating better agreement during autumn. The model simulation and satellite observations exhibit similar seasonal cycles of  $XCO_2$  with a small discrepancy over the Southern Africa and during wet seasons over all regions.

## 5 1 Introduction

An understanding of the regional contributions and trends of carbon dioxide ( $CO_2$ ) is critical to design mitigation strategies aimed at stabilizing atmospheric greenhouse gases. The present-day concentration of atmospheric  $CO_2$  continues to rise. Ongoing emissions of  $CO_2$  and other greenhouse gases will influence the global climate system during the next decades and centuries. Approximately one-half of the  $CO_2$  emissions from human activities is accumulating in the Earth's atmosphere, whereas the remaining portion of emitted  $CO_2$  is absorbed by sink on land and in the ocean (Raupach et al., 2007).

Several studies (e.g., Tsutsumi et al., 2009; Stocker, 2014; Allison, 2015) have shown that the column averaged dry air mole fractions of  $CO_2$  ( $XCO_2$ ) has undergone rapid changes from pre-industrial period value of 280 ppm to 396 ppm as recently as 2013. This change has been attributed to anthropogenic factors such as fossil fuel combustion, land use change, biomass burning, emission from industries such as cement. Notably, this value exceeds the highest  $XCO_2$  level retrieved from ice cores representing the past 800,000 years. This increasing trend has been persistent. For example according to the World Meteorological Organization (WMO) 2016 report, the average concentrations of  $CO_2$  hit 403.3 ppm, up from 400 ppm in 2015 surpassing an annual positive increasing rate of  $1.99 \pm 0.43 \text{ ppm yr}^{-1}$  (<http://www.esrl.noaa.gov/gmd/ccgg/trends/global.html> Houghton, 2007). These positive trends have led to imbalance of  $0.58 \pm 0.15 \text{ Wm}^2$  in energy budget between 2005 and 2010 at the top of the atmosphere (Hansen et al., 2011). To this end, changes in atmospheric temperature, hydrology, sea ice, and sea levels are attributed to climate forcing agents dominated by  $CO_2$  (Santer et al., 2013; Stocker et al., 2013). However, understanding the climate response to anthropogenic forcing in a more traceable manner is still difficult due to a major uncertainty in carbon-climate feedbacks (Friedlingstein et al., 2006). Part of this uncertainty is due to lack of sufficient data on regional and global carbon cycle. This is compounded with inappropriate modelling practices to capture spatio-temporal variability of carbon cycle. These problems can be solved through strengthening carbon monitoring networks and setting up proper modelling. A transport model, with appropriate physical and mathematical formulations and sufficiently tuned by observations, can be used to understand the spatio-temporal nature of atmospheric  $CO_2$  source and sink as well its associated drivers.

Towards this, a number of national and international efforts have been initiated in the recent past by different government and non-government agencies across the globe. Among these efforts, ground-based observations of greenhouse gas using Total Carbon Column Observing Network (TCCON) is a notable one since it provides accurate and high-frequency measurements of column-integrated  $CO_2$  mixing ratio. For example, it has been established that TCCON has a precision of 0.25% for measurements taken under clear sky conditions (Wunch et al., 2011). However, the number of TCCON sites is limited and can not establish accurate  $CO_2$  amount and flux on subcontinental or regional scale. Moreover, some studies shows that the large

uncertainty is amplified due to uneven global distribution of TCCON sites (Gurney et al., 2002; Hungershoefer et al., 2010). In addition, none of these ground based observation networks are found in Africa.

On the other hand, the  $CO_2$  concentration retrieved from the satellite-based  $CO_2$  absorption spectra have the advantages of unified, long-term, and the global coverage observation as compared to ground-based measurements. It has been established from theoretical studies that accurate and precise satellite derived atmospheric  $CO_2$  can appreciably minimize the uncertainties in estimated  $CO_2$  surface flux (Rayner and O'Brien, 2001; Chevallier, 2007). Other studies have revealed that significant improvement in estimation of weekly and monthly  $CO_2$  fluxes can be achieved subject to  $CO_2$  retrieval error of less than 4 ppm from satellite and modelling scheme whereby  $CO_2$  concentration is an independent parameter of carbon cycle model (Houweling et al., 2004; Hungershoefer et al., 2010). However,  $XCO_2$  shows temporal variability on different time scales: diurnal, synoptic, seasonal, inter-annual, and long term (Olsen and Randerson, 2004; Keppel-Aleks et al., 2011). More recent missions such as the Greenhouse gases Observing SATellite (GOSAT) (Hamazaki et al., 2005), the Orbiting Carbon Observatory-2 (OCO-2) (Boesch et al., 2011) and planned missions such as the Active Sensing of  $CO_2$  Emissions over Nights, Days, and Seasons (ASCENDS) (Dobbs et al., 2008) have been and are being developed specifically to resolve surface sources and sinks of  $CO_2$  and provide information on these different scales of temporal variability. For example, GOSAT observations started in 2009 and provide  $XCO_2$  based on spectra in the Short-Wavelength InfraRed (SWIR) region with a standard deviation of about 2 ppm with respect to ground-based and in-situ air-borne observations (Yokota et al., 2009; NIES GOSAT Project, 2012).

Moreover, atmospheric transport model, such as the NOAA Carbon Tracker (CT) is an integrated modelling system that assimilate  $CO_2$  from other observations in order to compliment satellite observations in understanding  $CO_2$  surface sources and sinks as well as its spatio-temporal variabilities. However, both satellite and model data should be validated against other independent satellite observations and/or in-situ observations before using them to answer scientific questions. As a result, a number of validation and intercomparison have been conducted in previous studies. For example, Kulawik et al. (2016) found root mean square deviation of 1.7, and 0.9 ppm in GOSAT and CT2013b  $XCO_2$  relative to TCCON respectively. Other authors have undertaken validation exercises and found bias of  $-8.85 \pm 4.75$  ppm in NIES  $XCO_2$  with respect to TCCON (Morino et al., 2010); root mean square deviation of  $-1.48$  and  $2.09$  ppm in NIES Level 2 V02.xx  $XCO_2$  (Yoshida et al., 2013); and bias of  $-0.68 \pm 2.56$  ppm in NIES level 2 V02.xx  $XCO_2$  with respect to aircraft observations (Inoue et al., 2013). Moreover, strong consistency between the ACOS and NIES  $XCO_2$  monthly averages time series over different regions was reported. For example, Deng et al. (2016a) found the greatest mean difference ( $1.43 \pm 0.60$  ppm) over China and the least over Brazil ( $-0.03 \pm 0.64$  ppm) in the two time series of monthly means. Globally, ACOS  $XCO_2$  is higher than NIES by about 1 ppm and has smaller bias than NIES data. Moreover, comparison of NIES Level 2 V02.xx  $XCO_2$  with  $XCO_2$  from Goddard Earth Observing System-Chemistry model(GEOS-5 v09-01-01) simulations revealed that the satellite  $XCO_2$  was lower than the model by 2 ppm on average globally (Lei et al., 2014). Liang et al. (2017) compared  $XCO_2$  from OCO-2 and GOSAT with that of TCCON and found mean measurement accuracy of 0.27 and -0.41 ppm with RMSD of 1.56 and 2.22 ppm respectively. However, they found the measurement accuracy of GOSAT decreased to -0.62 ppm with RMSD of 2.3 ppm for period from 2014 to 2016. Liang et al. (2017) also indicates GOSAT shows a larger seasonal variability in describing

amplitudes than OCO-2, with greater amplitude in the northern hemisphere than the southern hemisphere. Lei et al. (2014) also showed regional difference of  $XCO_2$  between the ACOS and NIES datasets. For example, a larger regional difference from 0.6 to 5.6 ppm was obtained over China land region, while it is from 1.6 to 3.7 ppm over global land region and from 1.4 to 2.7 ppm over US land region. These findings suggest that it is important to assess how satellite and model  $XCO_2$  compare with each other over other regions.

Therefore, this paper aims to assess the performance of Carbon Tracker model in simulating observed  $XCO_2$  from GOSAT and OCO-2 satellites over Africa using various statistical metrics and identify weakness and strengths of the respective data sets. Moreover, the skill of the model in capturing the amplitudes and phases of observed seasonal cycles over different parts of the continent is evaluated and the consistence of the modelled spatio-temporal variability with the known seasonal climatology of the regions that determines carbon source and sink levels is assessed.

## 2 Data and Methodology

### 2.1 Carbon Tracker Model and Data

Carbon Tracker is an annually updated analysis of atmospheric carbon dioxide distributions and their surface fluxes (Peters et al., 2007). It is a data assimilation system that combines observed carbon dioxide concentrations from 81 sites around the world with model predictions of what concentrations would be based on a preliminary set of assumptions (“the first guess”) about sources and sinks for carbon dioxide. Carbon Tracker compares the model predictions with reality and then systematically tweaks and evaluates the preliminary assumptions until it finds the combination that best matches the real world data. It has modules for atmospheric transport of carbon dioxide via weather systems, photosynthesis and respiration, air-sea exchange, fossil fuel combustion and fires. Transport of atmospheric  $CO_2$  is simulated by using the global two-way nested transport model (TM5). TM5 is an off line atmospheric tracer transport model (Krol et al., 2005) driven by meteorology from the European Centre for Medium-Range Weather Forecasts (*ECMWF*) operational forecast model and from the ERA Interim reanalysis (Dee et al., 2011) to propagate surface emissions. TM5 is based on a global  $3^0 \times 2^0$  and a  $1^0 \times 1^0$  spatial grids over North America.

The data from CT (version:CT2015) (<http://carbontracker.noaa.gov>; Peters et al. (2007)) is used to extend aircraft profiles from the stratosphere to the top of the atmosphere (Inoue et al., 2013; Frankenberg et al., 2016) and to quantify co-location error (Kulawik et al., 2016). The older data versions have been used and also compared with different data sets over other parts of the globe in previous studies (Peters et al., 2007; Nayak et al., 2014; Kulawik et al., 2016; Krishnapriya et al., 2017). Most of the studies confirm that CT  $XCO_2$  captures observations reasonably well. In this study we use Carbon Tracker release version CT2016, here after (CT2016) and near real time version (CT-NRT.v2017). Both versions of NOAA CT provides 3 hourly  $CO_2$  mole-fractions data for global atmosphere at 25 pressure levels for a period covering 2000 to 2016. The data can be accessed freely at the public domain (<ftp://aftp.cmdl.noaa.gov/products/carbontracker>).

## 2.2 GOSAT measurements

GOSAT is the world's first spacecraft dedicated solely to measure the concentrations of carbon dioxide and methane, the two major greenhouse gases, from space. The spacecraft was launched successfully on January 23, 2009, and has been operating since then. GOSAT records reflected sunlight using three near-infrared band sensors. The field of view at nadir allows a circular footprint of about 10.5 km diameter (Kuze et al., 2009; Yokota et al., 2009; Crisp et al., 2012). GOSAT consists of two instruments. The sensors for the two instruments can be broadly labelled as thermal, near infrared and imager. The first two sensors are used as part of Fourier Transform Spectrometer for carbon monitoring which is referred to as TANSO-FTS while the imager for cloud and aerosol observations is referred to as TANSO-CAI. The details on spectral coverage, resolution, field of view, and different products of TANSO-FTS in the three SWIR bands can be found in a number of previous studies (Kuze et al., 2009; Saitoh et al., 2009; Yokota et al., 2009, 2011; Crisp et al., 2012; Nayak et al., 2014; Deng et al., 2016a, and references therein). In this study bias corrected ACOS B3.5 Lite  $XCO_2$  from GOSAT Level 2 (L2) retrieval based on the SWIR spectra of FTS observations and made available by Atmospheric  $CO_2$  Observations from Space (ACOS) of NASA is used. ACOS B3.5 Lite  $XCO_2$  has lower bias and better consistency than NIES GOSAT SWIR L2  $CO_2$  globally (Deng et al., 2016a). Therefore, our choice of the ACOS B3.5 Lite, here after (GOSAT)  $XCO_2$  is motivated by these differences.

## 15 2.3 OCO-2 measurements

OCO-2, the second world's full-time dedicated  $CO_2$  measurement satellite, was successfully launched by National Aeronautics and Space Administration (NASA) on 2 July 2014. OCO-2 measures atmospheric carbon dioxide with the accuracy, resolution, and coverage required to detect  $CO_2$  source and sink on global and regional scale. OCO-2 has three-band spectrometer, which measures reflected sunlight in three separate bands. The  $O_2$  A-band measures molecular absorption of oxygen from reflected sunlight near  $0.76 \mu m$  while the  $CO_2$  bands are located near  $1.61 \mu m$  and  $2.06 \mu m$  (Liang et al., 2017). In this study, bias corrected OCO-2  $XCO_2$  V7 lite level 2 covering the period from January 2015 to December 2016, here after referred to as OCO-2  $XCO_2$  are used. Due to scarcity of data, CT values from the two releases CT2016 for the year 2015 and CT-NRT.v2017 for the year 2016, here after (CT16NRT17) are employed in this study. The OCO-2 project team at Jet Propulsion Laboratory, California Institute of Technology, produced the OCO-2  $XCO_2$  data used in this study. The data can be accessed from NASA Goddard Earth Science Data and Information Service Center.

## 2.4 Methods

The GOSAT and CT model  $XCO_2$  time series used in this investigation spans five years, ranging from May 2009 to April 2014. Atmospheric  $CO_2$  concentrations of NOAA Carbon-Tracker have a global coverage with a  $3^0 \times 2^0$  Longitude/Latitude resolution which covers 428 grid points in our study area. Satellite observations, however, is different from model assimilation, and have gaps because of various reasons (e.g., cloud and the observational mode of satellite). As a result, there is no one to one spatio-temporal match between the two data sets. For example,  $CO_2$  products from the two dataset are not directly comparable since CT is a 3 hourly smooth and regular grid dataset whereas GOSAT  $XCO_2$  is irregularly distributed in space and time.

Thus, the CT  $CO_2$  is extracted on the time and location of GOSAT  $XCO_2$  data. Using the grid point of CT as a reference bin, the corresponding GOSAT  $XCO_2$  found within a rectangle of  $1.5^0 \times 1.5^0$  with centre at the reference bin and with temporal mismatch of a maximum of 3 hrs is extracted. Moreover, CT has higher vertical resolutions than GOSAT. As a result, the two can not be directly compared. It is customary to smooth the high resolution data (in this case CT) with averaging kernels and a priori profiles of the low resolution satellite measurements (in this case GOSAT). In addition, due to a difference between CT and GOSAT on the number vertical levels, CT  $CO_2$  is interpolated to vertical levels of GOSAT. The CT  $XCO_2$  ( $XCO_2^{model}$ ) used in the comparison is computed from the interpolated CT  $CO_2$  ( $CO_2^{interp}$ ), pressure weighting function ( $w$ ),  $XCO_2$  a priori ( $XCO_{2a}$ ), column averaging kernel of the satellites retrievals ( $A$ ) and a priori profile ( $CO_{2a}$ ) of the retrievals as per procedure discussed by Rodgers and Connor (2003); Connor et al. (2008); O'Dell et al. (2012); Chevallier (2015); Jing et al. (2018) and given as:

$$XCO_2^{model} = XCO_{2a} + \sum_i w_i A_i * (CO_2^{interp} - CO_{2a})_i \quad (1)$$

where  $i$  is the index of the satellite retrieval vertical level.

Correlation coefficients (R), bias and root mean square deviation (RMSD) are used to assess the level of agreement between the two data sets. The mean bias determines the average deviations in  $XCO_2$  between Carbon Tracker simulation and satellite observations. In this work the bias at the  $j^{th}$  grid point is computed as:

$$Bias_j = \frac{1}{n} \sum_{i=1}^n (S_i - O_i) \quad (2)$$

where  $S_i$  and  $O_i$  are CT and GOSAT  $XCO_2$  values over the  $j^{th}$  pixel at the  $i^{th}$  time respectively. To quantify the extent to which  $XCO_2$  of CT and GOSAT agree, the pattern correlations at the  $j^{th}$  grid point are computed as:

$$R_j = \frac{\frac{1}{n} \sum_{i=1}^n (S_i - \bar{S})(O_i - \bar{O})}{\sqrt{\frac{1}{n} \sum_{i=1}^n (S_i - \bar{S})^2} \sqrt{\frac{1}{n} \sum_{i=1}^n (O_i - \bar{O})^2}} \quad (3)$$

where  $\bar{S}$  and  $\bar{O}$  are the mean values of  $S_i$  and  $O_i$  over the  $j^{th}$  pixel. The root mean square deviation (RMSD) which shows the standard error of the model with respect to the observation at the  $j^{th}$  grid point is computed as:

$$RMSD_j = \sqrt{\frac{1}{n} \sum_{i=1}^n ((S_i - \bar{S}) - (O_i - \bar{O}))^2} \quad (4)$$

This study also applies categorical contingency table for evaluation of performance of CT2016 in capturing the different parts of observed  $XCO_2$  distribution.  $XCO_2$  is a continuous physical quantity for which categorical metrics are not applicable. In such cases, scatter plots are used as a means of visual inspection of the model skill with no quantitative information in terms of spatial distribution and magnitude of the scatter apart from a single standard deviation. Recently, extended categorical contingency table is proposed to overcome this drawback and assess whether a model simulation/satellite retrieval can capture or fail to capture observed physical quantity exceeding a specified quantile threshold. This procedure effectively reduces the

continuous physical quantity with two outcomes i.e., yes (capture) or no (fail). In this study, the skill of CT in correctly simulating whether the observed  $XCO_2$  values are above a selected threshold will be determined using the categorical metrics. The categorical metrics includes Quantile Bias (QBias), Quantile Probability of Detection (QPOD), Quantile False Alarm Ratio (QFAR), Quantile Critical Success Index (QCSI) also known as the Threat Score and quantile Categorical miss (QMISS). The

5 QBias is defined as the ratio of number of observations (satellite data, OBS) to simulations (Carbon Tracker, SIM) above a certain threshold. Mathematically, QPOD, QFAR, QMISS and QCSI are defined as

$$QPOD = \frac{NoHit}{NoMiss + NoHit} \quad (5)$$

$$QMISS = \frac{NoMiss}{NoMiss + NoHit} \quad (6)$$

10

$$QFAR = \frac{NoFalse}{NoHit + NoFalse} \quad (7)$$

and

$$QCSI = \frac{NoHit}{(NoHit + NoFalse + NoMiss)} \quad (8)$$

where  $NoHit = \sum_i^n (SIM_i | (SIM_i > t \& OBS_i > t))$  is the number of data detected by both simulation ( $SIM$ ) and observation ( $OBS$ ) above a threshold  $t$ ,  $NoMiss = \sum_i^n (OBS_i | (SIM_i \leq t \& OBS_i > t))$  is the number of data detected by observation but missed by simulation and  $NoFalse = \sum_i^n (SIM_i | (SIM_i > t \& OBS_i \leq t))$  refers to number of data available only from model above the threshold  $t$  and  $n$  is the number of exceedances.

QPOD quantifies the fraction of reference observations (in this case GOSAT observations) detected correctly by the simulation above a selected threshold. Meaningful values of QPOD ranges from 0 (zero agreement) to 1 (perfect agreement); QFAR identifies the fraction of events captured by simulation but not available in reference observations above the threshold. Sound values of QFAR is bounded by 0 to 1 with 0 implying perfect score. QCSI combines different aspects of the QPOD and QFAR to characterize the overall performance of the simulation in capturing observation. The QCSI is constrained to have values between 0 (zero agreement) to 1 (perfect agreement) by definition. QMISS quantifies events identified by reference observation but missed by the simulation. Therefore, by definition, quantile categorical miss ranges from 0 (perfect score) to 1 (zero agreement). More details about these categorical statistical metrics can be found in works by other authors (e.g., AghaKouchak et al., 2011; Wilks, 2011; AghaKouchak and Mehran, 2013, and references therein). Using similar coincidence criteria and statistical methods, CT16NRT17 and OCO-2  $XCO_2$  are also compared.

### 3 Results and discussions

#### 3.1 Comparison of $XCO_2$ mean climatology from NOAA CT2016 and GOSAT

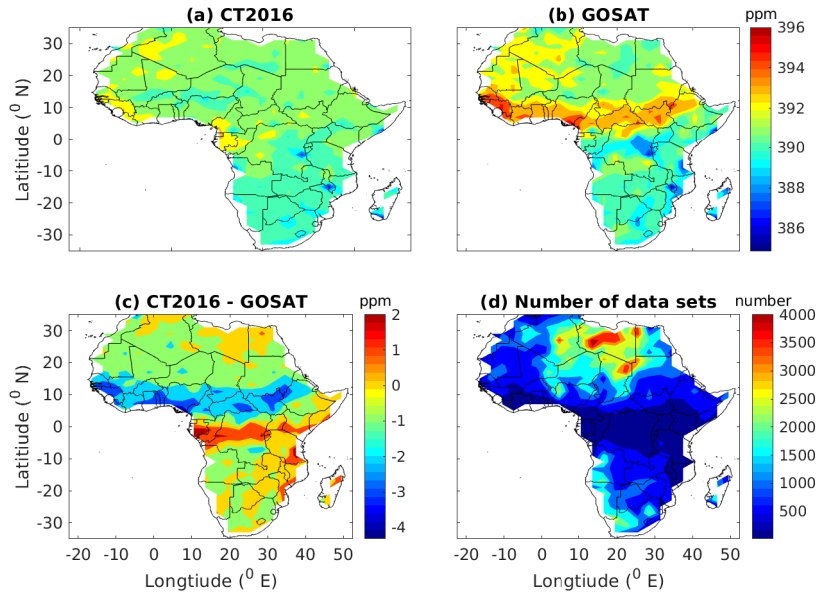
The mole fraction of  $CO_2$  obtained from the NOAA Carbon Tracker model and GOSAT observation was compared. The results are based on 426 grid points uniformly distributed to cover the whole Africa's land region. The analysis was based on five years daily data starting from May 2009 to April 2014. The  $XCO_2$  comparison was done only when there are more than ten  $XCO_2$  retrievals that fulfils the spatio-temporal matching criteria defined in Section 2.4.

Fig. 1 shows temporal average of CT2016 (Fig. 1a) and GOSAT (Fig. 1b)  $XCO_2$  distribution. The major common spatial feature in the mean map of  $XCO_2$  from GOSAT and CT2016 reanalysis is dipole structure characterized by high  $XCO_2$  northward of equator and low  $XCO_2$  southward of equator with the exception of Congo basin which is characterized by spatially anomalous high  $XCO_2$ . The Southern Africa region is characterized by weak anthropogenic  $CO_2$  emission and high  $CO_2$  uptake by the vegetation. This contributed to the observed dipole distribution. Another important pattern is anomalous peak over annual average location of Inter-tropical convergence zone (ITCZ) (Fig. 1b) which appears to fade over Eastern Africa. This is in agreement with fact that carbon stocks and net primary production per unit land area are higher over Equatorial Africa and decrease towards northward and southward of the equator over arid environments (Williams et al., 2007). However, Fig. 1a shows that CT2016 has some limitations in simulating this spatial pattern in comparison to GOSAT.

Fig. 1c shows mean difference (CT2016–GOSAT)  $XCO_2$  which ranges from -4 to 2 ppm. The highest difference between the CT2016 and GOSAT  $XCO_2$  (as high as -4 ppm) is observed over Equatorial Africa, western Ethiopia and South Sudan which are also known for near-year-round rainfall and relatively dense vegetation. The regions are known for their rain forest. The likely explanation could be  $CO_2$  flux from respiration (photosynthesis) of forest in the region which is underestimated (overestimated) in the reanalysis. However, the mean (over five years) may also be slightly positively biased due to fewer observations as shown in Fig.1d. The strategy and methods for cloud screening in GOSAT retrievals could lead to smaller number of observation in the equatorial region (Crisp et al., 2012; O'Dell et al., 2012; Yoshida et al., 2013; Chevallier, 2015; Deng et al., 2016b). The number of datasets used for comparison range from 14 to 4288 from grid to grid with a spatial mean of 1109 data over the continent. Fig. 1c also shows CT2016 simulations are overall lower than the values of GOSAT observation over most regions with an exception in Gabon, Congo, southern Kenya and southern Tanzania where CT2016 simulations are higher than GOSAT observation by more than 1 ppm. The spatial distribution of global atmospheric  $CO_2$  is not uniform because of the irregularly distributed sources of  $CO_2$  emissions, such as large power plant and forest fire, and biospherical assimilation as clearly noted above.

Fig. 2a shows the histograms of differences of CT2016 and GOSAT  $XCO_2$ . The mean difference between CT2016 and GOSAT means is about -0.27 ppm with the standard deviation of 0.98 ppm indicating good regional consistency and low potential outliers. Moreover, a negative mean of the difference implies that  $XCO_2$  simulated from CT2016 is lower than that of GOSAT retrievals over Africa land mass.

Because of selection criteria which permits a difference of 3 degree long and wide, the two datasets are not exactly at the same point. The impact of the relative distance between them should be assessed before performing any statistical comparison.



**Figure 1.** Distribution of five-years averages of CT2016 (a) and GOSAT (b)  $XCO_2$  and their difference (c) gridded in  $3^0 \times 2^0$  bins over Africa's Land mass; and the total number of datasets at each grid (d).

Fig. 2b depicted color-coded scatter plot of CT2016 model simulation versus GOSAT to determine if the discrepancy between the data sets arise from spatial mismatch. The color code indicates the relative distance between the model and observation datasets. For these datasets the 50<sup>th</sup> percentile has a relative distance of 1.19<sup>0</sup> which means 50% of the data has a relative distance shorter than 1.19<sup>0</sup>. The maximum relative distance between them is 2.12<sup>0</sup>. However, there is no indication that this has been the case since the scatter is not a function of relative distance between the data sets. For example, data points with blue color with lowest location difference is scattered everywhere instead of along the 1:1 line. Furthermore, we found the bias of -0.26 ppm, correlation coefficient of 0.86 and RMSD of 2.19 ppm for datasets which has a relative distance shorter than 1.19<sup>0</sup>. On the other hand, the bias, correlation coefficient and RMSD are -0.33 ppm, 0.86 and 2.22 ppm for those which are longer than 1.19<sup>0</sup>. The above statistics was performed merely to test the influence of location mismatch.

Fig. 3 shows a statistical comparison of  $XCO_2$  from the CT2016 and GOSAT over Africa. The number of data used in this comparison are shown in Fig. 1d. As it is depicted in Fig. 3a, the bias ranges from -4 to 2 ppm with a mean bias of -0.28 ppm (see Table 1). A larger negative bias of about -2 ppm was found along the annual mean position of ITCZ. The correlation varies from 0.4 over some isolated pockets in Congo, Tanzania, Mozambique, Uganda and western Ethiopia to 0.9 over northern half of Africa northward of 13<sup>0</sup>N, Eastern Ethiopia and Kalahari Desert. Fig. 3b depicts correlation coefficient between GOSAT and Carbon Tracker  $XCO_2$ . The region with poor correlation also exhibits high RMSD as shown in Fig. 3c. To understand whether this discrepancy originates from model weakness alone, we have looked at the GOSAT posteriori estimate of  $XCO_2$  error, which are high over the same regions with high bias and RMSD between GOSAT and Carbon Tracker  $XCO_2$  (Fig. 3d).

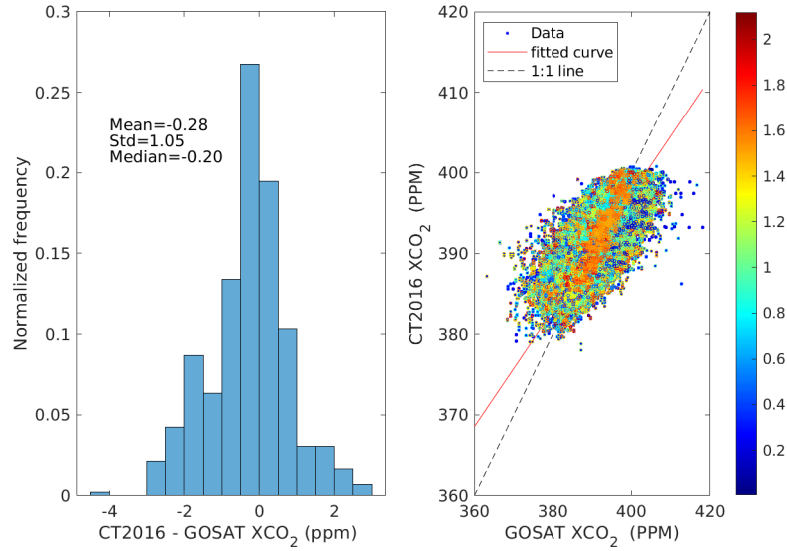


**Figure 2.** Histogram of the difference of CT2016 relative to GOSAT (left panel) and color code scatter diagram of  $XCO_2$  concentration as derived from CT2016 and GOSAT (right panel). Color indicates the relative distance as shown in colorbar between datasets.

GOSAT's posteriori estimate of  $XCO_2$  error is a combination of instrument noise, smoothing error and interference errors (Connor et al., 2008; O'Dell et al., 2012). This posteriori estimate of  $XCO_2$  error does not include forward model error which may lead to underestimation of the true error of satellite  $XCO_2$  by a factor of two (O'Dell et al., 2012). Therefore, part of the discrepancy is clearly linked to satellite own uncertainty, which might have been amplified due to small number of data points  
5 used to calculate the mean error of GOSAT  $XCO_2$  measurements (see Fig. 1d). In general, the two data sets are characterized by high spatial mean correlation of 0.83, a global offset of -0.28 ppm, which is the average bias, a regional precision of 2.30 ppm, and a relative accuracy of 1.05 ppm as depicted in Table 1.

**Table 1.** Summary of statistical relation between CT2016 and GOSAT observation. The statistical tools shown are the mean correlation coefficient (R), the spatial average of bias (Bias), the spatial average root mean square deviation (RMSD), the standard deviation in bias (std of Bias), GOSAT posteriori estimate of  $XCO_2$  error (GOSAT err), the standard deviation in CT2016  $XCO_2$  (CT2016 std) and the standard deviation in GOSAT  $XCO_2$  (GOSAT std). The number of data used in the statistics is 472,821 over 426 pixels covering the study period; distribution at each grid point is shown in Fig. 1d. Negative bias indicates that CT2016  $XCO_2$  is lower than GOSAT  $XCO_2$  values.

Statistical tool	R	Bias (ppm)	RMSD (ppm)	std of Bias (ppm)	GOSAT err (ppm)	CT2016 std (ppm)	GOSAT std(ppm)
Values	0.83	-0.28	2.30	1.05	0.91	0.90	1.55

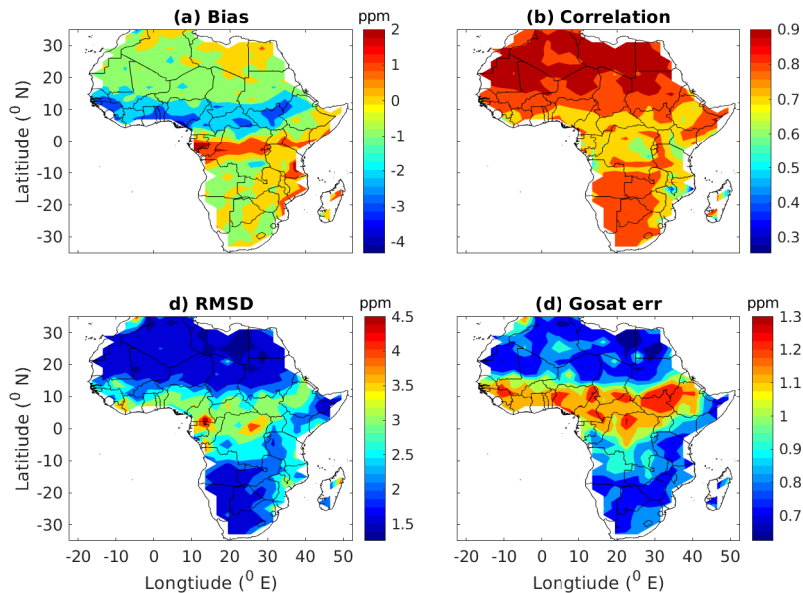


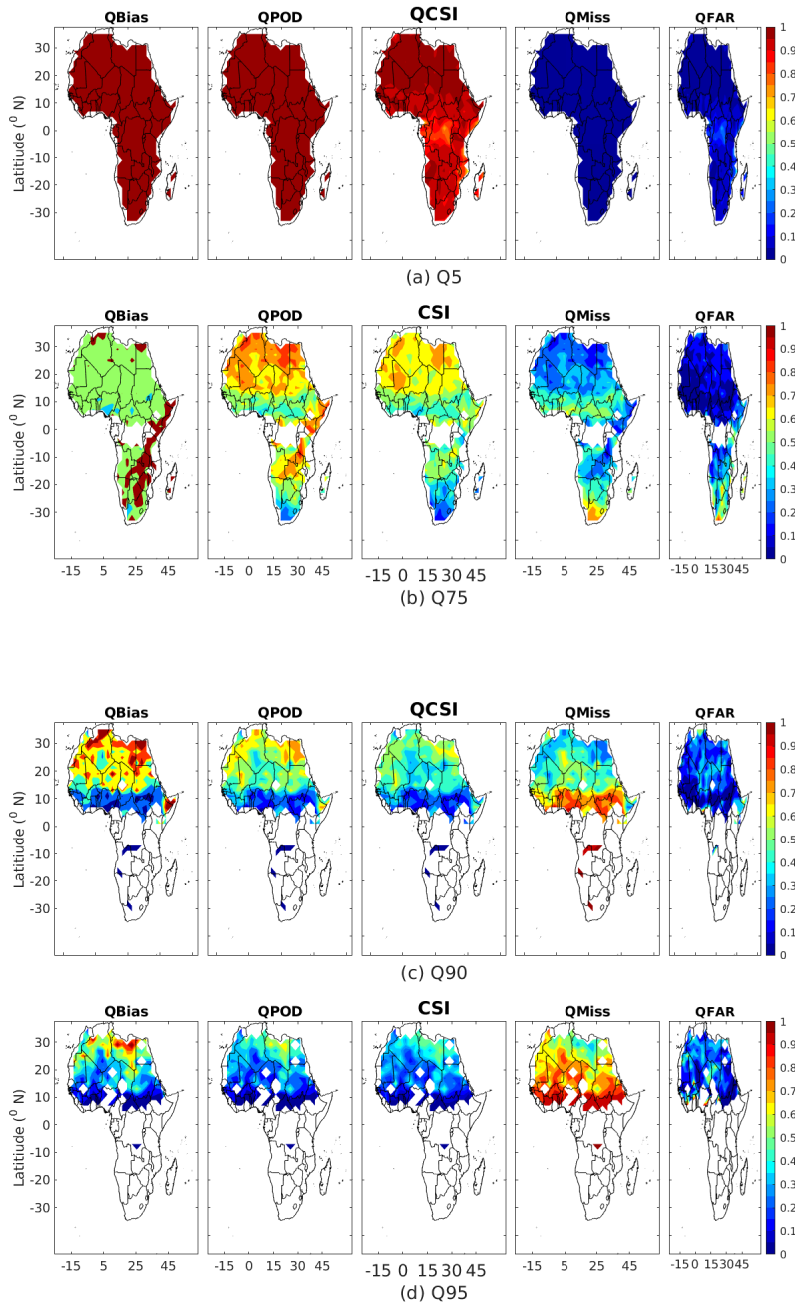
**Figure 3.** Spatial patterns of bias (a), correlation (b), RMSD (c) of the two data sets, and mean posteriori estimate of  $XCO_2$  error from GOSAT (d).

### 3.2 Categorical comparison of $XCO_2$ from NOAA CT and GOSAT

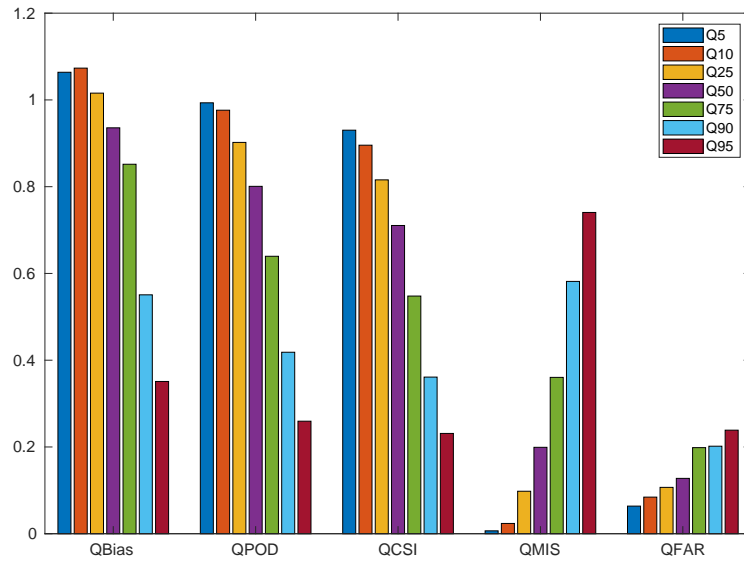
Following the methods described in AghaKouchak et al. (2011), QBias, QPOD, QCSI, QMISS and QFAR are determined from the coincident  $XCO_2$  data to assess how Carbon Tracker model and satellite observations perform with respect each other in capturing different parts of  $XCO_2$  distribution. It is worth noting that these categorical metrics are used to evaluate the level of agreement between CT2016 and GOSAT  $XCO_2$  in certain part of  $XCO_2$  distribution (e.g., above a given quantile threshold). In this way,  $XCO_2$  distribution is effectively rendered to be dichotomous variable for which we can use the categorical metrics.

Fig. 4 displays values for QBias, QPOD, QCSI, QMISS and QFAR for distribution exceeding 5% (first row), 75% (second row), 90% (third row) and 95% (fourth row) quantiles. We filter out pixels in which the total number of observations are less than 10 to avoid unreliable statistics. The thresholds are set based on the quantiles of the GOSAT observation. QPOD and QCSI decrease at higher quantiles. In contrast, QFAR and QMISS increase at higher quantiles. Specially the decrease in QCSI is significant. It ranges from 0.8 to 1.0 at 5<sup>th</sup> percentile ( i.e., QCSI for values exceeding the 5<sup>th</sup> percentile) and smaller than 0.4 at 90<sup>th</sup> percentile.

On the other hand, the QMISS which is below 0.07 at threshold of 5<sup>th</sup> percentile shows a value above 0.58 at threshold value of the 90<sup>th</sup> percentile for most of the regions (Fig. 4 ). This indicates that the agreement between CT2016 and GOSAT  $XCO_2$  deteriorates as the comparison data range includes only higher extremes of the  $XCO_2$  distribution. For example, on average over the continent at 95<sup>th</sup> percentile the QFAR is lower than 0.24 indicating that 24% (see also Table 2) of datasets



**Figure 4.** Distribution of categorical metrics over the study area for quantiles exceeding 5% (first row), 75% (second row), 90% (third row) and 95% (fourth row)



**Figure 5.** Summary of categorical metrics (QBias, QPOD, QCSI, QFAR and QMISS) averaged over Africa’s land region for 5, 10, 25, 50, 75, 90 and 95 percentile.

simulated by the model to be above 95<sup>th</sup> percentile threshold were not actually in the observation. This indicates that a notable difference between CT2016 and GOSAT  $XCO_2$  exists at the tails of the distribution. The information from these statistics are crucial for modelers and/or scientists working on satellite remote sensing to improve the model and/or the retrieval strategy. For example, in satellite retrievals, smoothing constraint or regularization (e.g., Tikhonov first or second order, the so called shape constraint) heavily penalizes the portion of the profile at low and high extremes thereby restricting the possibility of observing profiles unusually different from the a priori profile. It is worth-noting that the a priori profile is usually constructed from climatology of  $CO_2$  profile. In some case, only a handful of a priori profile represents a region (e.g., tropical model atmosphere, mid-latitude model atmosphere, polar model atmosphere) with wide range of variability. This could create huge discrepancy between the model and satellite observations in the tail region of the  $XCO_2$  distribution. The observed difference between CT and GOSAT may well be partly attributed to such factors. However, when the data covers lower extremes, QPOD and QCSI have substantially improved indicating the existence of better agreement between CT2016 and GOSAT at the lower end of the  $XCO_2$  distribution.

Fig. 4a shows the QPOD and QCSI are above 0.93 for lower quantiles which indicates that the model simulates above 93% of the observations (see also Table 2). However, at higher quantiles the change in contingency metrics show a clear deviation between the model simulation and observation. Figs. 4b show the scarce datasets in Equatorial Africa which, to certain extent, is the main reason for large biases observed around the Equator in Fig. 3a and also for the corresponding posteriori retrieval error in GOSAT  $XCO_2$  in Fig. 3d. Note that individual posteriori retrieval errors are smoothed out during averaging over large number of coincident observations. Fig. 4 shows that QBias is 1 at lower quantiles and decreases with increasing quantiles implying that the number of CT2016 data that matches the GOSAT observation decreases with increasing threshold. Fig. 4b

**Table 2.** Summary of extended contingency metrics for the relation between CT2016 model simulation and GOSAT observation.

Quantiles	QBias	QPOD	QCSI	QMISS	QFAR	threshold (ppm)	Number of grid points
Q5	1.064	0.993	0.93	0.007	0.064	384.32	424
Q10	1.073	0.976	0.896	0.024	0.084	385.73	421
Q25	1.016	0.902	0.816	0.098	0.107	388.17	419
Q50	0.936	0.801	0.711	0.199	0.128	391.27	405
Q75	0.852	0.64	0.548	0.36	0.198	394.52	386
Q90	0.551	0.418	0.361	0.582	0.202	397.31	284
Q95	0.351	0.259	0.231	0.741	0.239	398.98	225

shows a spatial mean bias of 0.85 (see also Table 2). Fig. 4b also depicts that QCSI is lower than 0.5 and the QMISS is above 0.3 over most regions of Southern Africa. However, QCSI exceeds 0.6 over regions northward of  $10^{\circ}N$ . The results indicates that, the agreement between CT2016 and GOSAT  $XCO_2$  shows a regional disparity which is better over Northern Africa than the Southern Africa. In general, the discrepancy between CT2016 and GOSAT  $XCO_2$  is significant over the whole continent towards the extreme high ends of the  $XCO_2$  distribution.

In addition, QBias, QPOD, QCSI, QMISS and QFAR are calculated for all data, i.e., data that includes values higher than 5, 10, 25, 50, 75, 90 and 95 percentiles and averaged over the whole African land mass, as shown in Fig. 5. There is one major conclusion that can be drawn from Fig. 5, i.e., the QFAR and QMISS increase with increase in the quantile thresholds while QBias, QPOD and QCSI decrease.

### 3.3 Comparison of monthly average time series of NOAA CT2016 and GOSAT $XCO_2$

Africa is one of the largest continents covering both northern and southern hemispheres. As a result, the continent is under the influence of semi-permanent high pressure cells which led to the Sahara Desert in the North and the Kalahari in the South. The equatorial low pressure cell which allows formation of the seasonally migrating inter-tropical convergence zone is part of the major large scale atmospheric circulation systems. These large scale pressure systems, Oceanic circulations and their interaction with the atmosphere coupled with diverse topographies of the region allow for the formation of different climates (e.g., equatorial, tropical wet, tropical dry, monsoon, semi desert (semi arid), desert (hyper arid), subtropical high climates). Geographically, the Sahel, a narrow steppe, is located just south of Sahara; the central part of the continent constitutes the largest rainforest next to Amazon whereas most southern areas contain savana plains. The continent get rainfall from migrating ITCZ, west Africa monsoon, intrusion of mid-latitude frontal systems, travelling low pressure systems (Mitchell, 2001, and references therein). Since  $CO_2$  fluxes exhibit seasonal variability and Africa experiences different seasons as noted above, it is important to divide Africa into three major regions, namely North Africa ( $10$  to  $35^{\circ}N$ ), Equatorial Africa ( $10^{\circ}S$  to  $10^{\circ}N$ ), and Southern Africa ( $35$  to  $10^{\circ}S$ ) and conduct the comparison of the two  $XCO_2$  datasets.

Figs. 6 - 8 show time series of  $XCO_2$  monthly means covering the period from May 2009 to April 2014 for both CT2016 and GOSAT over North Africa, Equatorial Africa and Southern Africa respectively. Figs. 6a - 8a depict the existence of an

**Table 3.** Summary of statistical relation between CT2016 and GOSAT observation. The statistical analysis were made using monthly average of time series of 60 months (i.e., months from May 2009 to April 2014).

Statistics	R	Bias (ppm)	RMSD (ppm)	number of data
Africa	0.997	-0.254	0.265	698505
North Africa	0.996	-0.361	0.345	424070
Equatorial Africa	0.977	-0.172	0.708	101660
Southern Africa	0.964	0.006	0.841	172775

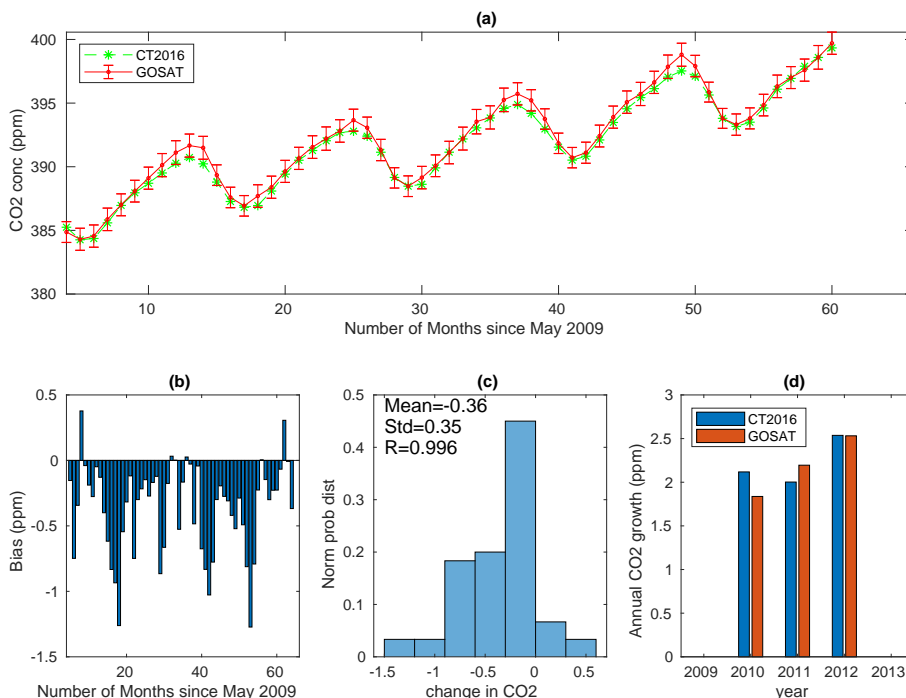


**Figure 6.** The monthly mean time series of CT2016 and GOSAT from May 2009 to April 2014 averaged over North Africa (a), bias associated to the monthly means (b), the histogram of difference (c) and the annual growth rate obtained by subtracting the mean from the mean of the next year (d). The error bars in (a) shows the GOSAT a posteriori  $XCO_2$  uncertainty.

overall very good agreement for the monthly averages with respect to amplitudes and phase of  $XCO_2$ . However,  $XCO_2$  from the two data sets slightly disagree in capturing seasonal cycle over Southern Africa.

Fig. 6a shows that  $XCO_2$  concentration reaches maximum (394.79 ppm) for CT2016 and (395.35 ppm) for GOSAT in April and minimum in September (388.66 ppm) for CT2016 and (388.75 ppm) for GOSAT over North Africa. Consistent with this evidence, other authors (e.g., Zhou et al., 2008) have indicated presence of a strong absorption of  $CO_2$  by vegetation during August in the northern hemisphere. This is also likely cause for minimum  $XCO_2$  observed during September over North Africa. The largest monthly mean difference of -0.90 ppm between the two datasets is observed in June, while the smallest

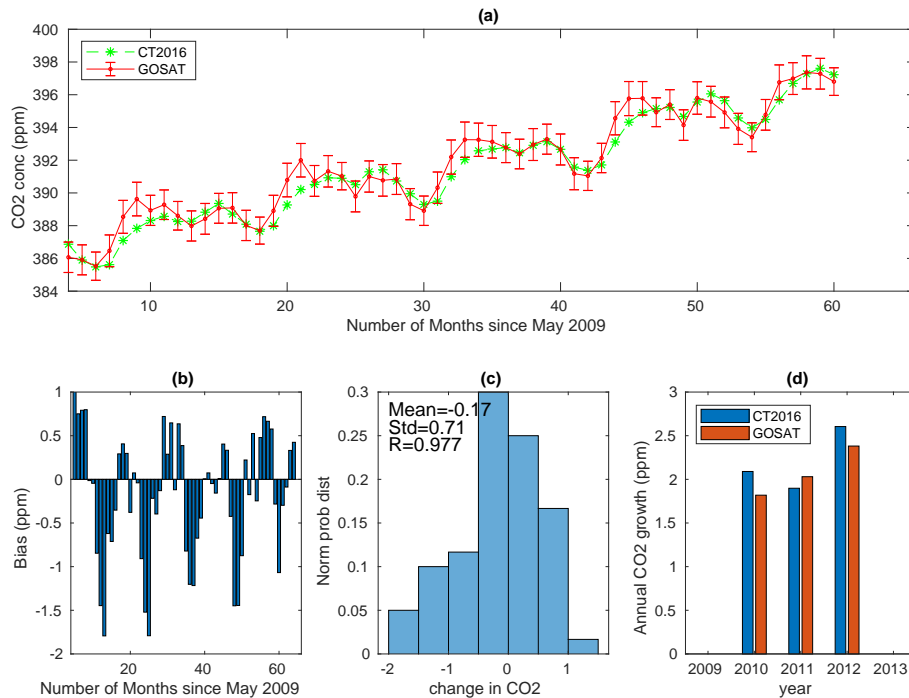


**Figure 7.** The same as Fig. 6 but over Equatorial Africa.

value of -0.04 ppm is found in August (see also Table 4). In addition, both datasets show  $XCO_2$  increases from October to April and decreases from May to September. Moreover, the two dataset shows a monthly mean regional mean bias of -0.36 ppm with a correlation of 1.0 and root mean square deviation of 0.36 ppm (see Table 3).

Fig. 7a shows  $XCO_2$  concentration reaches maximum (392.99 ppm) for CT2016 in March and (393.53 ppm) for GOSAT in January while minimum (389.56 ppm for CT2016 and 389.32 ppm for GOSAT) in October over Equatorial Africa. The largest monthly mean difference of -1.34 ppm and the smallest of -0.05 ppm between the two datasets observed in December in April respectively (Table 4). Moreover, both datasets show that  $XCO_2$  increases from October to March while it decreases from June to October. This similarity in the seasonal variability of the two datasets shows that they are in good agreement in terms of amplitude and phase. In addition, the two data sets show a monthly average regional average bias of -0.17 ppm, correlation of 0.98 and a small root mean square deviation 0.71 ppm over Equatorial Africa (see Table 3). Fig. 8a shows maximum  $XCO_2$  concentration in April (391.04 ppm) for CT2016 and in October (391.28 ppm) for GOSAT, while minimum in May (389.30 ppm) for CT2016 and ( 388.46 ppm) for GOSAT over Southern Africa. The largest monthly mean difference of 1.53 ppm and 0.03 ppm between the two datasets is observed in April and in July (Table 4) respectively. Both datasets show concentration of  $CO_2$  increases from May to July while it decreases from October to November. However, the  $XCO_2$  from CT2016 shows a gradual increasing trend from January to April. Conversely, GOSAT  $XCO_2$  shows a decreasing trend. This is most likely

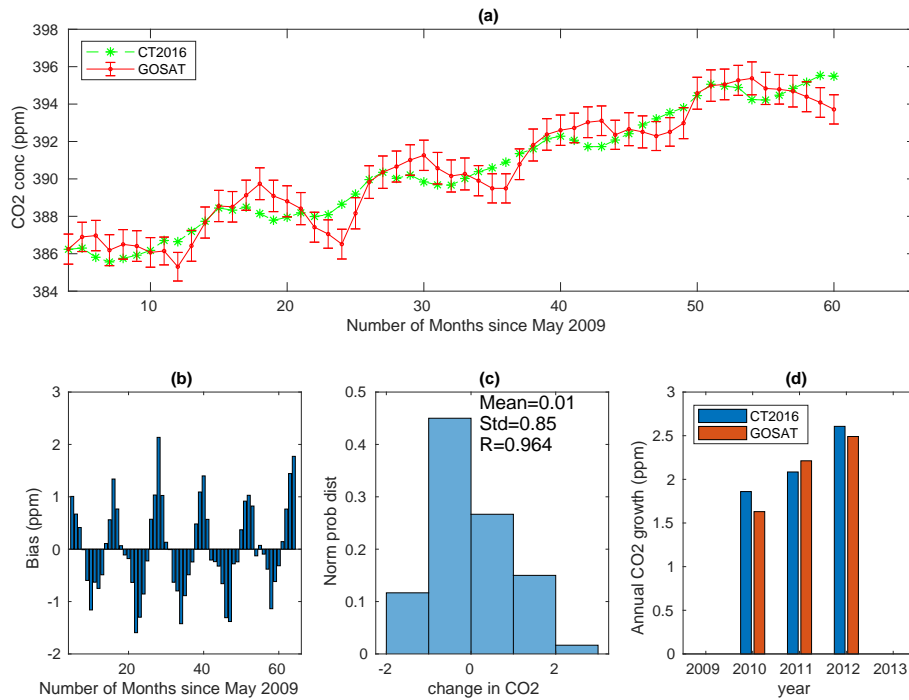


**Figure 8.** The same as Fig. 6 but over Southern Africa.

CT2016 simulation respond to the growing size of sinks following the rainy season. Moreover, the two data sets shows a monthly mean regional mean bias of 0.07 ppm, correlation of 0.97 and RMSD of 0.87 ppm over southern Africa (see Table 3).

Figs. 6b - 8b show regional averaged bias in the monthly mean  $XCO_2$  time series between CT2016 and GOSAT covering the period of May 2009 to April 2014. Fig. 6b shows the presence of seasonally varying negative bias over North Africa. A high ( $<-0.5$  ppm) negative bias in dry seasons (April to June) and low ( $\geq -0.1$  ppm) negative bias in wet seasons (August to September) are observed. Moreover, the strength of bias increases from February to June. Conversely, the bias decreases from June to September. Similarly, Figs. 7b and 8b show seasonally fluctuating bias over Equatorial and Southern Africa regions. For example, Fig. 8b shows a positive bias from February to July and negative bias from August to December over Southern Africa.

Figs. 6c - 8c show the histogram of difference. The mean difference between CT2016 simulation and GOSAT observation of  $XCO_2$  is -0.36 ppm with a standard deviation of 0.35 ppm over North Africa (see Fig. 6c); Fig. 7c presents a mean difference of -0.17 ppm with standard deviation of 0.71 ppm over Equatorial Africa; and Fig. 8c reveals a mean difference of 0.01 ppm and a standard deviation of 0.85 ppm which indicate that  $XCO_2$  from CT2016 was slightly higher than that of GOSAT over Southern Africa on average. In addition, the low standard deviation of monthly mean difference over North Africa typically indicates good regional consistency between CT2016 and GOSAT. This is mainly because Northern Africa is dominated by the Sahara desert which is known for its weak source/sink of  $CO_2$ . However, the spatial mean of monthly mean bias is slightly

**Table 4.** Five years monthly averaged  $XCO_2$  concentration in ppm obtained from CT2016 (CT) and GOSAT (GO) and their difference  $CT - GO$  (D) in ppm over Africa (A), North Africa (NA), Equatorial Africa(EA) and Southern Africa (SA).

Month	A CT	A GO	A D	NA CT	NA GO	NA D	EA CT	EA GO	EA D	SA CT	SA GO	SA D
January	391.81	392.17	-0.36	392.43	392.61	-0.18	392.22	393.53	-1.31	390.28	390.49	-0.21
February	392.48	392.58	-0.1	393.27	393.5	-0.23	392.72	393.21	-0.49	390.52	390.06	0.46
March	393.25	393.28	-0.03	394.02	394.29	-0.27	392.99	393.19	-0.2	390.82	389.81	1.01
April	393.81	393.91	-0.1	394.79	395.35	-0.56	392.87	392.92	-0.05	391.04	389.51	1.53
May	391.65	391.85	-0.21	392.92	393.73	-0.81	390.47	389.93	0.54	389.3	388.46	0.84
June	391.49	391.94	-0.45	392.43	393.33	-0.9	391.12	390.89	0.23	389.95	389.85	0.11
July	390.92	391.1	-0.18	391.09	391.5	-0.41	391.44	391.03	0.41	390.43	390.4	0.03
August	389.89	389.96	-0.07	389.4	389.44	-0.04	390.92	390.72	0.21	390.37	390.61	-0.25
September	389.26	389.4	-0.14	388.65	388.75	-0.1	390.02	389.67	0.35	390.39	391.01	-0.61
October	389.19	389.71	-0.51	388.85	389.26	-0.41	389.56	389.32	0.24	389.95	391.28	-1.32
November	389.97	390.43	-0.46	390.06	390.32	-0.26	389.86	390.52	-0.66	389.8	390.76	-0.96
December	391.09	391.53	-0.45	391.42	391.6	-0.18	391.23	392.57	-1.34	389.98	390.52	-0.54

higher (-0.36 ppm) over North Africa than over Equatorial Africa (-0.17 ppm ) and Southern Africa (0.01 ppm). This is likely due to the presence of strong local source from emissions and long range transport from the Northern Hemisphere as reported in other studies (Williams et al., 2007; Carré et al., 2010).

Figs. 6d - 8d display annual growth rate of  $XCO_2$  which ranges from 1.5 to 2.7  $ppm\ yr^{-1}$ . Moreover, the two datasets are consistent in determining the annual growth rate. The results are found in good agreement with the observed variability in the globally annual growth rate from surface measurements (<http://www.esrl.noaa.gov/gmd/ccgg/trends/global.html>) which is 1.67, 2.39, 1.70, 2.40, 2.51  $ppm\ yr^{-1}$  global during 2009 - 2013 respectively, and 1.89, 2.42, 1.86, 2.63, 2.06  $ppm\ yr^{-1}$  for Mauna Loa during 2009 - 2013 respectively, with error bars of 0.05 - 0.09  $ppm\ yr^{-1}$  for global and 0.11  $ppm\ yr^{-1}$  for Mauna Loa data sets(Kulawik et al., 2015). The growth rate may not be conclusive due to short length of the data sets used. However, it reflects how the CT and GOSAT observations perform with respect to each other.

### 3.4 Comparison of seasonal climatology

Seasonal cycle has important implications for flux estimates (Keppel-Aleks et al., 2012). It is important to analyse whether there are seasonally dependent biases that are affecting the seasonal cycle, and whether the data sets are capturing the same seasonal cycle. The four seasons considered here are: winter (December, January and February or in short DJF), spring (March, April and May or in short MAM ), summer (June, July and August or in short JJA), and autumn (September, October and November or in short SON). Fig. 9 shows the seasonal distributions of CT2016 (left panels) and GOSAT (middle panels)  $XCO_2$  and their difference (CT2016 - GOSAT, right panels). The distribution clearly shows that  $XCO_2$  concentration is maximum during spring (MAM) and minimum during autumn (SON) over the North Africa. On the other hand maxima is found during autumn

(SON) and minima during winter (DJF) over the Southern Africa. These features are in good agreement with the rainfall climatology of northern and southern hemispheres. Moreover, Table 5 shows seasonally varying biases. Seasonal biases affect the seasonal cycle and amplitudes, which are important for biospheric flux attribution (Lindqvist et al., 2015).

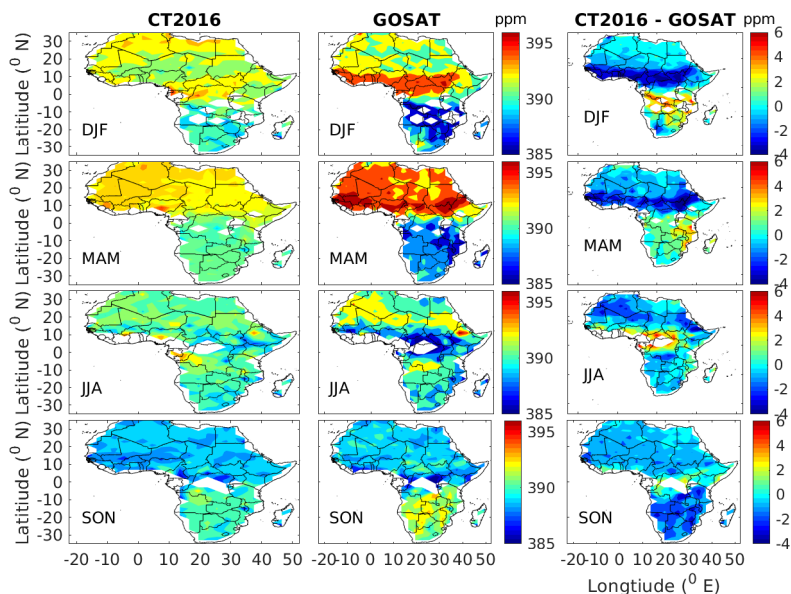


**Figure 9.** Seasonal climatology of  $XCO_2$  for NOAA CT2016 (left panels) and GOSAT (midel panels) and their difference (right panels).

The right panels in Fig. 9 show that the seasonal mean difference (CT2016 - GOSAT) ranges from -4 to 6 ppm. A maximum difference of 6 ppm over the gulf of Guinea and Congo during JJA. However, such maximum difference was observed over Southern Africa during DJF. A minimum of -4 ppm over annual mean ITCZ region was observed during DJF and MAM. Moreover, the difference is above 1 ppm over Southern Africa regions during DJF and MAM (wet season of the region). This implies high spatial variability in the seasonal mean difference (see also Table 5). It also suggests that the discrepancy between the CT2016 and GOSAT becomes significant when vegetation cover is weak during DJF and MAM (dry seasons) over North Africa.

During SON the seasonal difference in most Africa's land region ranges from -2 to 1 ppm. The result implies CT2016 simulates lower values of  $XCO_2$  than that of GOSAT observation indicating that there is a better spatial consistency during this season. Furthermore, during these seasons both the Northern and Southern Africa have a moderate vegetation cover following their respective summer seasons. The two datasets show lower regional variation (i.e., only from -2 to 2 ppm) over most of Africa land mass. However, the Equatorial Africa exhibits the mean difference lower than -2 ppm during DJF and MAM. This indicates the model tends to simulate lower than GOSAT retrievals  $XCO_2$  over the region. In addition, this strong negative bias is partially due to positive bias in GOSAT  $XCO_2$  retrieval due to cirrus clouds. For example, O'Dell et al. (2012) noted that GOSAT  $XCO_2$  retrievals are positively biased due to thin cirrus clouds. Fig. 9 (right panels) reveals  $XCO_2$  from CT2016

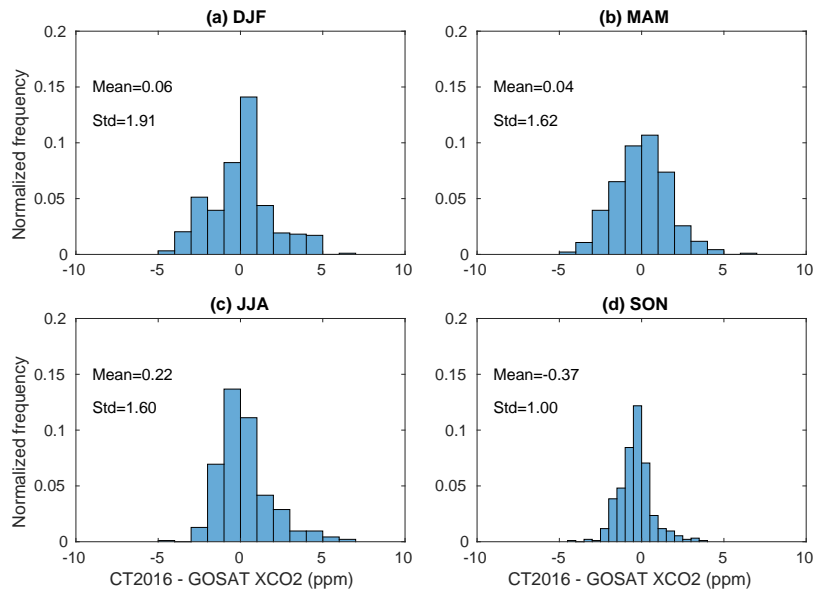


**Figure 10.** Histogram of difference for the seasonal  $XCO_2$  climatology for DJF (a), MAM(b), JJA (c) and SON (d) seasons.

is lower than GOSAT  $XCO_2$  over Northern Africa. The underestimation of observed  $XCO_2$  by NOAA CT2016 model is likely related with the skill of driving ERA-Interim data as noted from previous studies. For example, Mengistu Tsidu (2012) has shown that the ERA-Interim data has a wet bias over Ethiopian highlands. Mengistu Tsidu et al. (2015) have also shown that ERA-Interim precipitable water is higher than measurements from radio-sonde, FTIR and GPS observations. Therefore, such wet bias in the driving ERA-Interim GCM might have forced NOAA CT2016 to generate dense vegetation which serve as  $CO_2$  sink. In other study, Nagarajan and Aiyyer (2004) found ECMWF has a cold bias in the lower atmosphere between 1000 to 750 hPa against independent upper-air sounding data which may affects  $CO_2$ .

Fig. 10 shows mean difference between CT2016 and GOSAT  $XCO_2$  seasonal means which ranges from -0.37 to 0.04 ppm with a standard deviation within a range of 1.00 to 1.91 ppm over the continent. The highest mean difference of  $XCO_2$  (-0.37 ppm) occurs during SON and the lowest (0.04 ppm) occurs during MAM. Table 5 presents the summary of statistical values for spatial mean of each season mean. The comparison between the two data sets also shows there is a strong correlation (>0.5) during each season over the continent. However, there is moderate correlations (0.3 to 0.5) during DJF and MAM over North Africa and during DJF over Southern Africa. The low correlation over Northern Africa may be linked to a weak absorption by vegetation and a strong emission from human activities during winter as reported elsewhere (Liu et al., 2009; Kong et al., 2010). Moreover, Table 5 shows that the seasonal biases are negative over North Africa while they are mostly positive over Equatorial and Southern Africa. Negative biases are observed during DJF and SON over Equatorial and Southern Africa respectively implying that  $XCO_2$  from CT2016 are lower than GOSAT during dry seasons.

**Table 5.** Summary of statistical relation between CT2016 and GOSAT  $XCO_2$ : Bias, correlation (R), Root mean square deviation (RMSD), standard deviation of  $XCO_2$  from CT2016 simulation (CT2016 std), standard deviation of  $XCO_2$  from GOSAT observation (GOSAT std), aggregate number of coincident observations (number of data) and number of grids over the region (grid). Negative bias means CT2016 is lower than GOSAT. The statistics are on the basis of spatial average of seasonal averages of bias, correlation, RMSD and standard deviations.

Region	Statistics	Bias (ppm)	R	RMSD (ppm)	CT2016 std (ppm)	std in GOSAT (ppm)	number of data	grid
Africa	DJF	0.06	0.73	1.91	1.15	2.57	135865	409
	MAM	0.04	0.92	1.62	1.98	3.25	95942	410
	JJA	0.22	0.65	1.59	1.12	2.08	116360	400
	SON	-0.37	0.76	1	0.94	1.52	124233	408
North Africa	DJF	-0.25	0.36	1.08	0.67	1.12	103913	204
	MAM	-0.72	0.44	1.11	0.62	1.24	65115	204
	JJA	-0.42	0.73	1.17	0.9	1.66	60854	204
	SON	-0.35	0.66	0.53	0.52	0.71	91778	204
Equatorial Africa	DJF	-0.52	0.68	2.47	1.06	3.07	22639	121
	MAM	0.18	0.9	1.88	1.94	3.46	8300	115
	JJA	1.51	0.59	2.02	1.46	2.52	12714	104
	SON	0.25	0.7	1.3	1.16	1.83	10213	113
Southern Africa	DJF	1.61	0.42	1.72	0.88	1.9	9313	84
	MAM	1.56	0.67	0.97	0.82	1.31	22527	91
	JJA	0.18	0.81	0.78	0.93	1.31	42792	92
	SON	-1.16	0.77	0.81	0.84	1.26	22242	91

### 3.5 Comparison of mean $XCO_2$ from NOAA CT16NRT17 and OCO-2

The strong El Niño event occurred during 2015-2016 provides an opportunity to compare the performance of CT16NRT17 during strong El Niño events. Because of the decline in terrestrial productivity and enhancement of soil respiration, the concentration of  $CO_2$  increases during El Niño events (Jones et al., 2001). In this section we compare mean  $XCO_2$  of NOAA CT16NRT17 and NASA's OCO-2 covering the period from January 2015 to December 2016. OCO-2 is the most recent full-time dedicated  $CO_2$  measuring satellite with greater spatio-temporal resolution.

The comparison was done based on the selection criteria discussed in Section 2.4. Fig. 11 shows mean distribution of  $XCO_2$  from CT16NRT17 (Fig. 11a) and OCO-2 (Fig. 11b) over Africa's land mass. CT16NRT17 shows high ( $> 400$  ppm)  $XCO_2$  values over North Africa while these high  $XCO_2$  values are observed over Equatorial Africa in the case of OCO-2

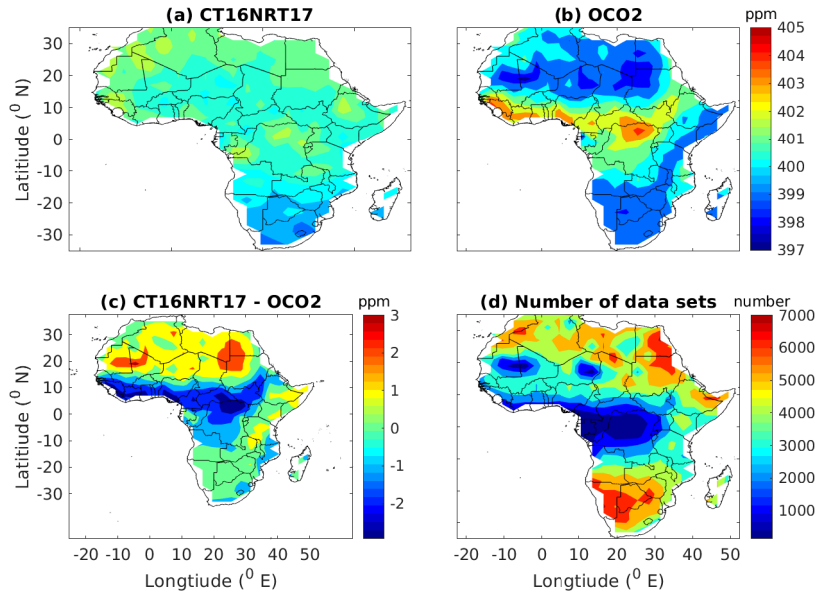


**Figure 11.** Distribution of two years average  $XCO_2$  of CT16NRT17 (a) and OCO-2 (b)  $XCO_2$  and their difference (c) gridded in  $3^0 \times 2^0$  bins; and (d) the total number of datasets at each grid

observation. The two datasets show a discrepancy over Equatorial Africa, where CT16NRT17 simulates low  $XCO_2$  values ( $< 401$  ppm) while OCO-2 observes high values of  $XCO_2$  ( $> 401$  ppm). Both datasets show moderate  $XCO_2$  values which ranges from 397 to 400 ppm over Southern Africa. The  $XCO_2$  distribution from OCO-2 is consistent with the maximum  $CO_2$  concentration reported in past study (Williams et al., 2007) implying that the CT16NRT17 likely underestimates  $XCO_2$  values

5 over Equatorial Africa. It is also possible that the discrepancy is a compounded effect of OCO-2  $XCO_2$  positive bias over the region (O'Dell et al., 2012; Chevallier, 2015). Fig. 11c shows the mean difference between two years mean of  $XCO_2$  from CT16NRT17 and OCO-2, which is in the range from -2 to 2 ppm. However, high ( $< -2$  ppm) negative mean difference between the two data sets over rain forest regions (Gulf of Guinea and Congo basin) and ITCZ zone over Eastern Africa (South Sudan and southeastern Sudan) is observed implying that CT16NRT17 simulates lower  $XCO_2$  values than that of OCO-2 observation

10 over regions where vegetation uptake is strong. Conversely, high ( $> 1$ ) positive mean difference over the Sahara desert, Somalia and Tanzania implies CT16NRT17 simulates higher  $XCO_2$  values than OCO-2 observation where the vegetation uptake is weak. Moreover, a positive ( $> 2$ ) mean difference over Egypt, Libya, Sudan, Chad, Niger, Mali and Mauritania is likely due to overestimates of  $XCO_2$  emission from local sources by CT16NRT17. Overall, the two datasets show a fairly reasonable agreement with a correlation of 0.60 and offset of 0.36 ppm, a regional precision of 2.51 ppm and a regional accuracy of 1.21

15 ppm.

**Table 6.** Summary of statistical relation between CT16NRT17 and OCO-2 observation. The statistical tools shown are the mean correlation coefficient (R), the average of bias (Bias), the average root mean square deviation (RMSD), the standard deviation in bias (std of Bias), mean posteriori estimate of  $XCO_2$  error from OCO-2 (OCO-2 err), the standard deviation in CT16NRT17  $XCO_2$  (CT16NRT17 std) and the standard deviation in OCO-2  $XCO_2$  (OCO-2 std). Positive Bias indicates that CT16NRT17 is higher than OCO-2. The number of data used in the statistics is 1,659,411 over 426 pixels covering the study period. Distribution at each grid point is shown in Fig 11d.

Statistical tool	R	Bias (ppm)	RMSD (ppm)	std of Bias (ppm)	OCO-2 err (ppm)	CT16NRT17 std (ppm)	OCO-2 std (ppm)
Values	0.6	0.34	2.57	1.21	0.55	0.55	1.28

Fig. 12a shows the histogram of two years mean difference, which is characterized by a positive mean of 0.34 ppm and a standard deviation of 1.21 ppm. This suggests that CT16NRT17 simulates high  $XCO_2$  as compared to observations from OCO-2 over Africa's land mass.

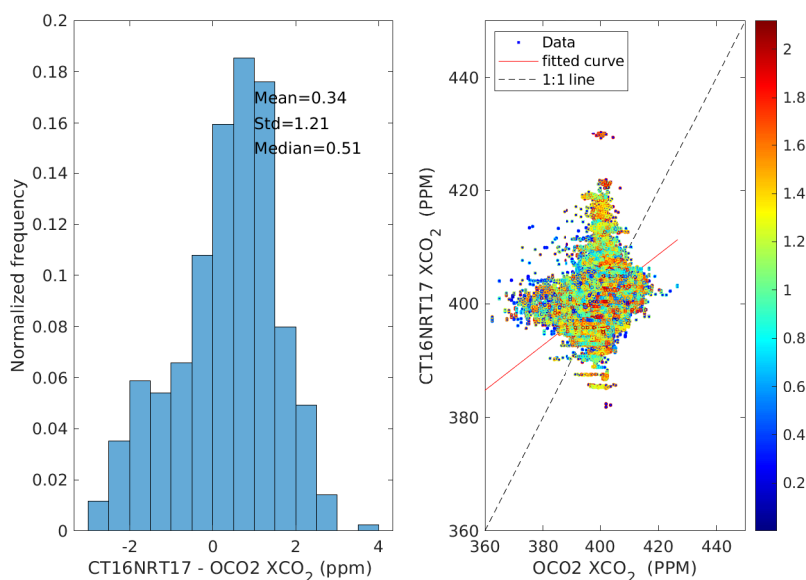


**Figure 12.** Histogram of the difference of CT16NRT17 relative to OCO-2 (left panel) and color code scatter diagram of  $XCO_2$  concentration as derived from CT16NRT17 and OCO-2 (right panel). Color indicates the relative distance as shown in colorbar between datasets.

Because of presence of spatial and temporal mismatch of some level between CT16NRT17 and OCO-2 datasets, it is important to assess the effect of relative distance between the datasets. Fig. 12b shows a color coded distribution of the two datasets. In the figure color codes indicate the relative distance. The random scatter of blue dots implies that the statistical discrepancies do not arise from the relative distance between the two datasets. More specifically, a statistical comparison of datasets lower

and higher than the 50<sup>th</sup> percentile (1.2<sup>0</sup>) shows bias of 0.58 and 0.57 ppm, correlation of 0.57 and 0.57 and RMSD of 2.65 and 2.67 ppm respectively.

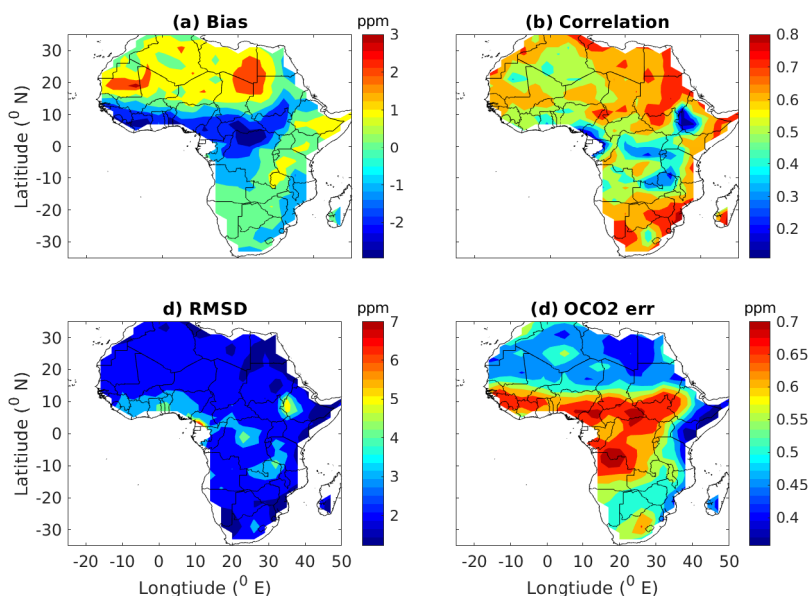


**Figure 13.** The bias (a), correlation (b), RMSD (c) of model and OCO-2  $XCO_2$  and mean posteriori estimate of  $XCO_2$  error from OCO-2 (d).

Fig. 13 shows the comparison of mean  $XCO_2$  from CT16NRT17 and OCO-2 covering the period from January 2015 to December 2016. The number of data used are displayed in Fig. 11d. Fig. 13a depicts the bias which ranges from -2 to 2 ppm with a mean bias of 0.34 ppm. However higher biases (<-2 ppm) are observed over Equatorial Africa along the annual average location of ITCZ. Fig. 13b shows the correlation map with values from 0.2 to 0.8 over Africa's land mass. A good correlation exceeding 0.6 are seen over many regions of the continent while weak correlation of less than 0.2 and higher root mean square error (> 3 ppm) are observed over small pockets of Equatorial and Eastern Africa regions (see Fig. 13c). These regions also show high (> 0.65 ppm) error in satellite retrieval (see Fig. 13d). In addition, Fig. 11d shows the number of observations are small (< 1000) over the regions. This may contribute to the observed discrepancy over these regions. However, weak correlations are also observed over a wider area in North Africa such as Mauritania, Mali, Algeria and some regions of Niger where satellite errors are low and sufficient data are obtained. This indicates the necessity of incorporating more measurement in Carbon Tracker assimilation over North Africa in order to tune the assimilation model such that it captures the sub-regional carbon cycles. The poor correlation and high RMSD values observed over Ethiopia highland is likely due to the inefficiency of retrieving  $XCO_2$  from satellites over high-latitude lands (Chevallier, 2015).

### 3.6 Categorical comparison of $XCO_2$ from NOAA CT16NRT17 and OCO-2

Fig. 14 depicts the QBias, QPOD, QCSI, QMISS and QFAR between CT16NRT17 and OCO-2 at different thresholds. The maps clearly show that QFAR and QMISS increase with increasing threshold. On the other hand, QBias, QPOD and QCSI decrease with increasing thresholds (see also Fig. 15).

5 In our analysis, threshold is determined based on OCO-2 observation. The value of  $XCO_2$  at 90<sup>th</sup> percentile is 404.25 ppm and most CT16NRT17  $XCO_2$  value are below 404 ppm over North Africa. Therefore, categorical analysis shows white space over these regions for thresholds above 90<sup>th</sup> percentile. Fig. 14 also shows that CT16NRT17 simulates the observation at lower quantiles. However, discrepancy between CT16NRT17 and OCO-2 is significant at higher quantiles. At 75<sup>th</sup> quantile the QPOD and QCSI values are less than 0.6 over Africa's land mass which implies more than 40% of the OCO-2 observation  
10 were not captured in the CT16NRT17 simulation.

### 3.7 Comparison of monthly average time series of NOAA CT16NRT17 and OCO-2 $XCO_2$

Figs. 16 - 18 show a two year monthly average time series comparison of  $XCO_2$  from CT16NRT17 and OCO-2 over North Africa, Equatorial Africa and Southern Africa respectively. Fig. 16a shows the existence of good agreement between the two datasets in describing pattern over North Africa. Moreover, both datasets show a decreasing trend of  $XCO_2$  from May  
15 to September while increasing trend from October to April. On the other hand, consistent with the climate condition and associated  $CO_2$  exchange, the monthly mean  $XCO_2$  shows a maximum value of 403.37 ppm for CT16NRT17 and 402.06 ppm for OCO-2 during May. Conversely, a minimum concentration of 398.77 ppm from CT16NRT17 simulation and 398.27 ppm from OCO-2 observation are found in September. In addition, both CT16NRT17 and OCO-2 show maximum  $XCO_2$  values (402.15 ppm for CT16NRT17 and 402.03 ppm for OCO-2) in December. These pick values in December are not  
20 surprising, because the 2015-2016 El Niño started on March 2015 and reached pick in December 2015 which added extra  $CO_2$  into the atmosphere (Chatterjee et al., 2017). Fig. 16a also shows that  $XCO_2$  from CT16NRT17 simulation are higher than OCO-2 observation over North Africa.

Fig. 16b shows the monthly mean difference between CT16NRT17 and OCO-2 which ranges from -0.5 to 2 ppm. As a consequence of strong El Niño, the region misses the short rain season during spring (MAM) when vegetation are still under  
25 the influence of the dormancy of winter (DJF). However, following the summer vegetation awakens from the long dormancy and becomes a sink of  $CO_2$ . Starting from August 2015, the difference between the two datasets is minimum; this implies that CT simulates low values of  $XCO_2$  when the vegetation uptake is strong. On the other hand, a maximum difference of exceeding 1 ppm was observed during MAM, implying higher  $XCO_2$  values from CT16NRT17 simulation than that of OCO-2 when vegetation uptake is weak following the strong El Niño over North Africa. Moreover, Fig. 16c displays a monthly mean  
30 regional mean bias of 0.87 ppm, correlation of 0.95 and a root mean square deviation of 0.72 ppm between CT16NRT17 and OCO-2  $XCO_2$ . This implies that CT16NRT17 is in a good agreement with OCO-2. However, a small discrepancies arose due to likely a strong anthropogenic emission from Nigeria, Egypt and Algeria together with the establishment of plantation over

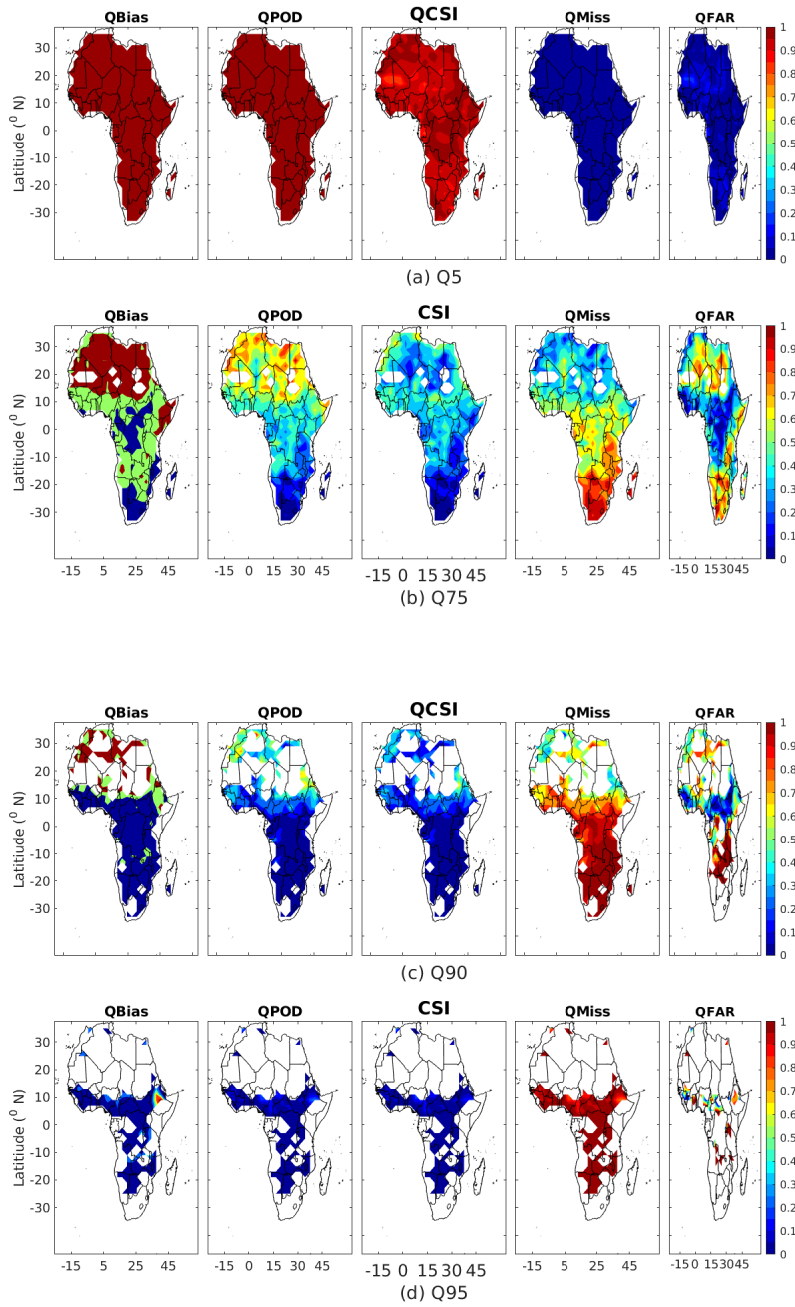


**Figure 14.** Distribution of categorical metrics over the study area for quantiles exceeding 5% (first row), 75% (second row), 90% (third row) and 95% (fourth row).

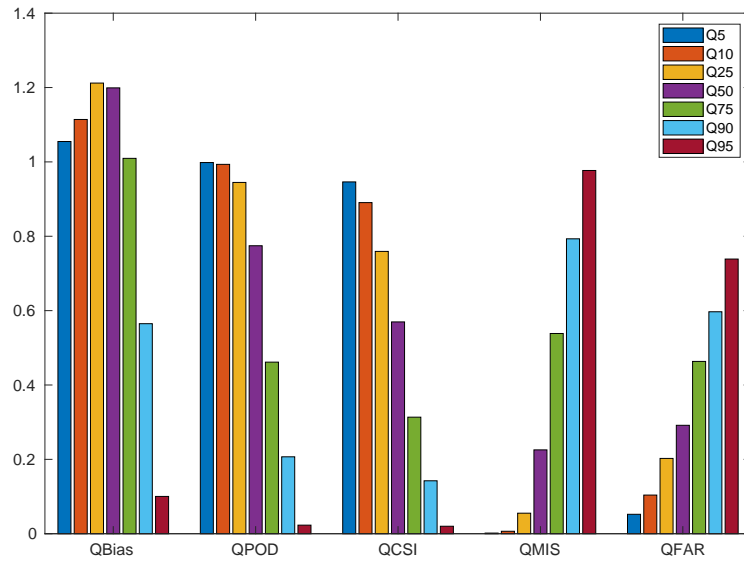


**Figure 15.** Summary of categorical metrics (QBias, QPOD, QCSI, Qmis and QFAR) averaged over Africa's land region for 5, 10, 25, 50, 75, 90 and 95 percentiles.

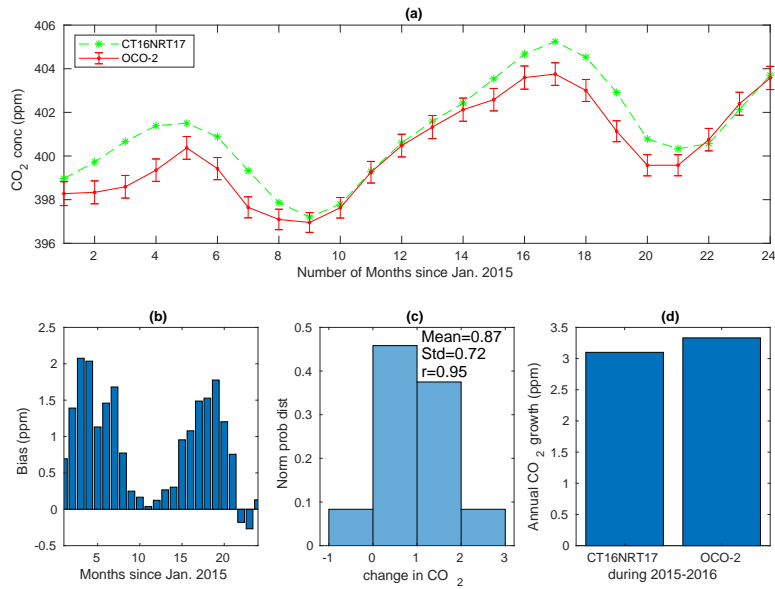


**Figure 16.** The monthly mean time series of CT16NRT17 and OCO-2 from January 2015 to December 2016 averaged over North Africa (a), bias associated to the monthly means (b), the histogram of difference (c) and the annual growth rate obtained by subtracting the mean from the mean of the next year (d). The error bars in (a) shows the OCO-2 a posteriori  $XCO_2$  uncertainty.

North Africa, which recently exceeded deforestation, and resulted in net flux of carbon sink (Canadell et al., 2009). This might have contributed to the observed discrepancy over North Africa.

Figs. 17a - 18a show monthly mean time series of  $XCO_2$  from the model and OCO-2 instrument over Equatorial Africa and Southern Africa which are also in good agreement in terms of pattern. However, the figures show that CT16NRT17 simulations are lower than those of OCO-2 during October, November and December whereas it is opposite during April, May and June over Equatorial Africa and Southern Africa. Figs. 17b and 18b depict a seasonal bias in the monthly time series over Equatorial Africa and Southern Africa respectively. Positive biases are observed during dry seasons while negative biases are during wet seasons. Moreover, the datasets have monthly averaged regional mean biases of 0.13 and 0.11 ppm, correlation of 0.90 and 0.94, RMSD of 0.84 and 0.73 ppm over Equatorial Africa and Southern Africa respectively. This shows that existence of better agreement between CT16NRT17 and OCO-2 over these regions in terms of monthly average regional mean values. Figs. 16d-18d show both CT16NRT17 and OCO-2 are in good agreement in estimating the annual growth rate. Patra et al. (2017) found a global mean of more than 3 ppm of  $CO_2$  added to the atmosphere due to the strong El Niño event that occurred during 2015-2016. In agreement with this, both CT16NRT17 and OCO-2 shows an annual growth rate that ranges from 3.10 to 3.42 ppm year<sup>-1</sup> of  $XCO_2$  over Africa's land mass (see also Table 7). However, over all regions of Africa's land mass CT16NRT17 shows lower  $XCO_2$  annual growth rate than those of OCO-2.

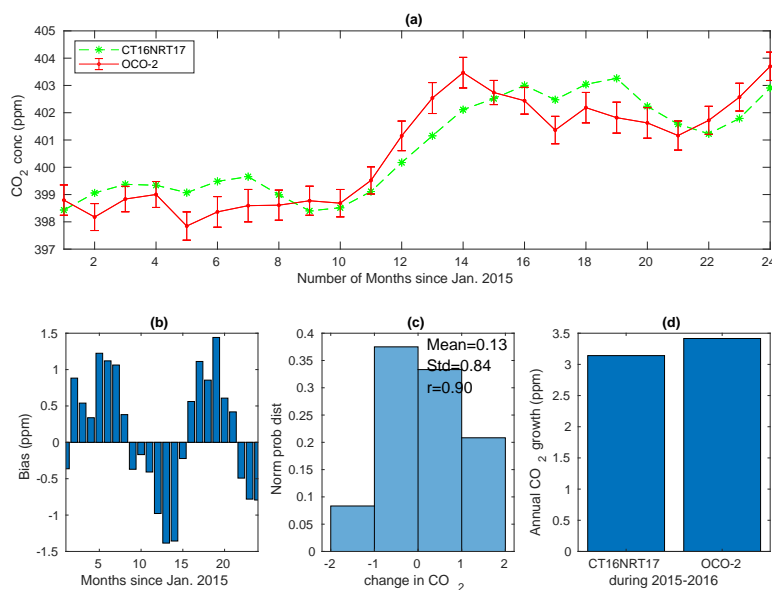


**Figure 17.** The same as in Fig. 16 but over Equatorial Africa.

### 3.8 Comparison of seasonal means of NOAA CT16NRT17 and OCO-2 $XCO_2$

Fig. 19 depicts seasonal means of  $XCO_2$  over Africa's land mass from CT16NRT17 (left panels), OCO-2 (middle panels) and their difference (right panels) covering period of January 2015 to December 2016. The white space seen over some regions

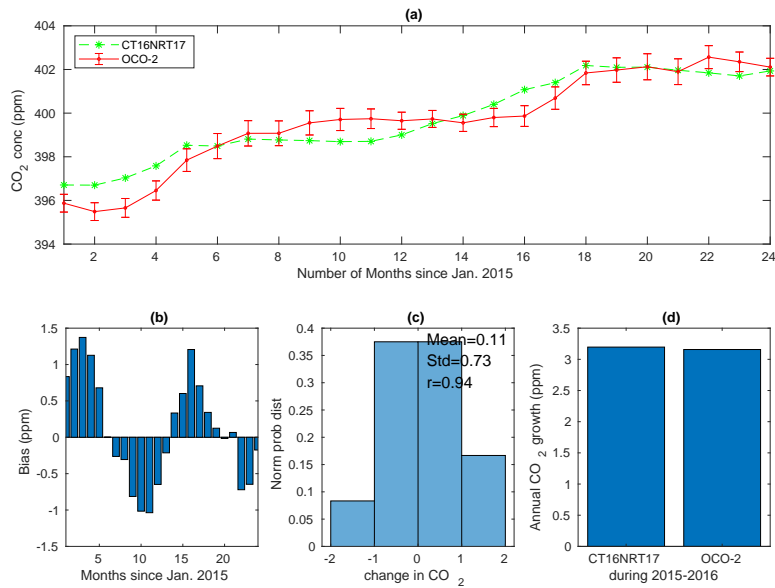


**Figure 18.** The same as in Fig. 16 but over Southern Africa.

**Table 7.** Annual growth rate (AGR) of  $XCO_2$  over Africa land mass from CT16NRT17 and OCO-2. The results are obtained as the mean annual difference of 2015 and 2016 values

Region	AGR of CT ( $\text{ppm year}^{-1}$ )	AGR Of OCO-2 ( $\text{ppm year}^{-1}$ )
North Africa	3.10	3.33
Equatorial Africa	3.14	3.42
Southern Africa	3.20	3.16

(e.g., Mali during JJA) is due to insufficient coincident satellite data according to the selection criteria during these seasons.  $XCO_2$  increases from winter to spring and then decreases from spring peak to summer minimum over the whole continent. The decrease from spring maximum to summer continued into autumn over northern half of Africa in contrast to southern half of Africa which exhibits an increase in  $XCO_2$ . The decrease from spring to autumn (northward of equator) and until summer (southward of equator) is likely to be a consequence of the land vegetation awakening from dormancy of winter and partly spring. Conversely, the decomposition of died and decayed vegetation which began in autumn and continued throughout winter adds extra  $CO_2$  leading to a maximum concentration during spring (Idso et al., 1999). In agreement with this, both CT16NRT17 and OCO-2 show maximum  $XCO_2$  during MAM over North Africa and during SON over Southern Africa. Conversely, minimum  $XCO_2$  are observed during SON over North Africa and during DJF over South Africa.

Fig. 19 (right panels) shows the seasonal mean difference of CT16NRT17 and OCO-2. A higher mean difference of greater than 1 ppm are observed over North Africa during DJF and MAM when the vegetation cover over the region decreases. This indicates that  $XCO_2$  values from CT16NRT17 are higher than that of OCO-2 when vegetation uptake is weak. On the other

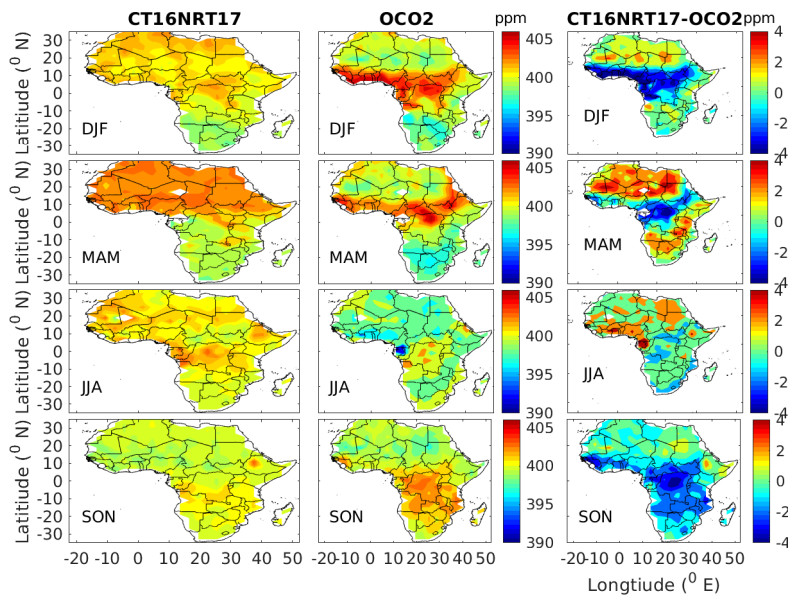


**Figure 19.** Seasonal mean of  $CO_2$  for NOAA CT16NRT17 (left panels) and OCO-2 (middle panels) and their difference (right panels).

hand, higher negative mean difference of less than -2 ppm are observed over Equatorial Africa during DJF and during SON over Southern Africa. This difference between the CT and OCO-2 arises likely during forest fire that naturally occurs following their respective dry season. Consistent with report by Liang et al. (2017), low seasonal variability is observed between CT16NRT17 and OCO-2 in the range from -4 to 4 ppm with greater amplitude over North and Equatorial Africa than over Southern Africa (see Figs. 19 (right panels)).

Fig. 20 shows the histogram of seasonal mean difference of CT16NRT17 and OCO-2. The smaller standard deviation of 1.49 and 1.07 are observed during JJA and SON. On the other hand, higher standard deviation of 1.69 and 1.75 ppm are observed during DJF and MAM respectively. The results indicate that CT16NRT17 and OCO-2 show a better consistency during wet seasons and this consistency decreases as the vegetation cover decreases over most regions of Africa land mass during dry seasons.

#### 4 Conclusions

In this study, the NOAA CT2016  $XCO_2$  values are compared with two full-time  $CO_2$  dedicated satellites, GOSAT and OCO-2 over Africa land mass. Comparison between CT2016 and GOSAT were done using a five years datasets covering the period from May 2009 to April 2014. This comparison is important to test the performance of CT2016 in capturing climatology of the  $XCO_2$ . Comparison of CT16NRT17 with OCO-2 was done using two years data during the strong El Niño event from January 2015 to December 2016. This provide opportunity to assess the performance of CT16NRT17 simulation during strong El Niño

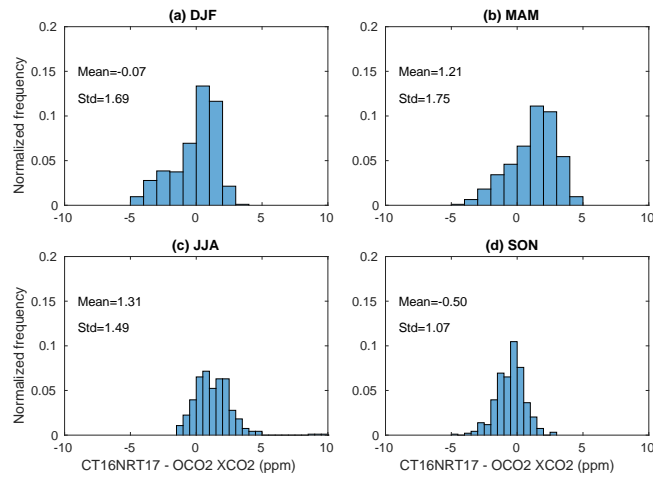


**Figure 20.** Histogram of difference for the seasonal  $CO_2$  climatology for DJF (a), MAM(b), JJA (c) and SON (d) seasons.

events. Comparison of Carbon Tracker with the two satellites reveals biases of -0.28 and 0.34 ppm, correlations of 0.83 and 0.60 and root mean square deviations of 2.30 and 2.57 ppm with respect to GOSAT and OCO-2 respectively. The performance of the model in capturing the whole distribution is also assessed. It is found that Carbon Tracker can capture more than 93% of the observation higher than the lowest ( $5^{th}$  percentile) thresholds. However, the quantile probability of detection and the

5 quantile critical success index decrease with increasing threshold implying the model and satellite show some discrepancies over the extreme values exceeding  $90^{th}$  percentile.

The monthly average time series of CT2016 over North Africa, Equatorial Africa and Southern Africa are separately compared with  $XCO_2$  from the two satellites. CT2016 agrees well with measurements from the two instruments in terms of pattern and amplitude. However, this agreement deteriorates over Equatorial and Southern Africa in terms of amplitude. It is

10 also found that there is a seasonal dependent bias between them which is negative during dry seasons while it is positive during wet seasons. This indicates results of CT2016 are mostly lower than the GOSAT observation. High spatial mean of seasonal mean RMSD of 1.91 during DJF and 1.75 ppm during MAM and low RMSD of 1.00 and 1.07 ppm during SON in the model  $XCO_2$  with respect to GOSAT and OCO-2 are observed respectively thereby indicating better agreement between CT and the

15 satellites during autumn. CT2016 has the ability to capture monthly time series and seasonal cycles. However,  $XCO_2$  from CT2016 is lower than GOSAT observations over North Africa during all seasons whereas  $XCO_2$  from CT2016 is higher than that of GOSAT over Equatorial and Southern Africa with the exceptions of DJF over Equatorial Africa and SON over Southern Africa. In addition, CT2016 simulates lower  $XCO_2$  than the observations over some regions (e.g., Congo, South Sudan and southwestern Ethiopia) and during summer season over the whole continent following large vegetation uptake. In contrast,  $XCO_2$  from CT16NRT17 is higher than that of OCO-2 over North Africa whereas it is lower than that of OCO-2 during DJF

20 and SON over Equatorial and Southern Africa respectively.

In general,  $XCO_2$  from NOAA CT shows a very small bias with respect to GOSAT and OCO-2 observation over Africa's land mass. Moreover, there is a good agreement between CT simulation and observations in terms spatial distribution, monthly average time series and seasonal climatology. However, there are some discrepancies between the model and the two  $XCO_2$  datasets from GOSAT and OCO-2 implying that the accuracy of the model data needs further improvements for the rain forest regions (e.g., Congo) through assimilation of in-situ observations and tuning of the model through process studies. Further work may also be needed to improve the  $XCO_2$  from satellites and models in the extreme parts of  $XCO_2$  distribution.

*Acknowledgements.* The authors acknowledge NOAA Earth System Research Laboratory and NASA GOSAT for the data products. The first author also acknowledges Addis Ababa University, Addis Ababa Science and Technology University, Botswana International University of Science and Technology for their support through fellowship and access to the research facilities..

## References

- AghaKouchak, A. and Mehran, A.: Extended contingency table: Performance metrics for satellite observations and climate model simulations, *Water Resources Research*, 49, 7144–7149, 2013.
- AghaKouchak, A., Behrangi, A., Sorooshian, S., Hsu, K., and Amitai, E.: Evaluation of satellite-retrieved extreme precipitation rates across the central United States, *Journal of Geophysical Research: Atmospheres*, 116, 2011.
- Allison, I.: The science of climate change: questions and answers, Australian Academy of Science, pp. 1–44, 2015.
- Boesch, H., Baker, D., Connor, B., Crisp, D., and Miller, C.: Global characterization of CO<sub>2</sub> column retrievals from shortwave-infrared satellite observations of the Orbiting Carbon Observatory-2 mission, *Remote Sensing*, 3, 270–304, 2011.
- Canadell, J., Raupach, M., and Houghton, R.: Anthropogenic CO<sub>2</sub> emissions in Africa, *Biogeosciences*, 6, 463–468, 2009.
- Carré, F., Hiederer, R., Blujdea, V., and Koebler, R.: Background guide for the calculation of land carbon stocks in the biofuels sustainability scheme: drawing on the 2006 IPCC guidelines for national greenhouse gas inventories, Luxembourg: Joint Research Center, European Commission, EUR, 24573, 34463, 2010.
- Chatterjee, A., Gierach, M., Sutton, A., Feely, R., Crisp, D., Eldering, A., Gunson, M., O'dell, C., Stephens, B., and Schimel, D.: Influence of El Niño on atmospheric CO<sub>2</sub> over the tropical Pacific Ocean: Findings from NASA's OCO-2 mission, *Science*, 358, eaam5776, 2017.
- Chevallier, F.: Impact of correlated observation errors on inverted CO<sub>2</sub> surface fluxes from OCO measurements, *Geophysical Research Letters*, 34, 2007.
- Chevallier, F.: On the statistical optimality of CO<sub>2</sub> atmospheric inversions assimilating CO<sub>2</sub> column retrievals, *Atmospheric Chemistry and Physics*, 15, 11 133–11 145, 2015.
- Connor, B. J., Boesch, H., Toon, G., Sen, B., Miller, C., and Crisp, D.: Orbiting Carbon Observatory: Inverse method and prospective error analysis, *Journal of Geophysical Research: Atmospheres*, 113, 2008.
- Crisp, D., Fisher, B., O'Dell, C., Frankenberg, C., Basilio, R., Bosch, H., Brown, L., Castano, R., Connor, B., Deutscher, N., et al.: The ACOS CO<sub>2</sub> retrieval algorithm-Part II: Global XCO<sub>2</sub> data characterization, 2012.
- Dee, D. P., Uppala, S., Simmons, A., Berrisford, P., Poli, P., Kobayashi, S., Andrae, U., Balmaseda, M., Balsamo, G., Bauer, P., et al.: The ERA-Interim reanalysis: Configuration and performance of the data assimilation system, *Quarterly Journal of the royal meteorological society*, 137, 553–597, 2011.
- Deng, A., Yu, T., Cheng, T., Gu, X., Zheng, F., and Guo, H.: Intercomparison of Carbon Dioxide Products Retrieved from GOSAT Short-Wavelength Infrared Spectra for Three Years (2010–2012), *Atmosphere*, 7, 109, 2016a.
- Deng, F., Jones, D. B., O'Dell, C. W., Nassar, R., and Parazoo, N. C.: Combining GOSAT XCO<sub>2</sub> observations over land and ocean to improve regional CO<sub>2</sub> flux estimates, *Journal of Geophysical Research: Atmospheres*, 121, 1896–1913, 2016b.
- Dobbs, M., Dobler, J., Braun, M., McGregor, D., Overbeck, J., Moore, B., Browell, E., and Zaccheo, T.: A modulated CW fiber laser-lidar suite for the ASCENDS mission, in: Proc. 24th International Laser Radar Conference, 2008.
- Frankenberg, C., Kulawik, S. S., Wofsy, S. C., Chevallier, F., Daube, B., Kort, E. A., O'Dell, C., Olsen, E. T., and Osterman, G.: Using airborne HIAPER Pole-to-Pole Observations (HIPPO) to evaluate model and remote sensing estimates of atmospheric carbon dioxide, *Atmospheric Chemistry and Physics*, 16, 7867–7878, 2016.
- Friedlingstein, P., Cox, P., Betts, R., Bopp, L., von Bloh, W., Brovkin, V., Cadule, P., Doney, S., Eby, M., Fung, I., et al.: Climate-carbon cycle feedback analysis: results from the C4MIP model intercomparison, *Journal of climate*, 19, 3337–3353, 2006.

- Gurney, K. R., Law, R. M., Denning, A. S., Rayner, P. J., Baker, D., Bousquet, P., Bruhwiler, L., Chen, Y.-H., Ciais, P., Fan, S., et al.: Towards robust regional estimates of CO<sub>2</sub> sources and sinks using atmospheric transport models, *Nature*, 415, 626–630, 2002.
- Hamazaki, T., Kaneko, Y., Kuze, A., and Kondo, K.: Fourier transform spectrometer for greenhouse gases observing satellite (GOSAT), in: *Enabling sensor and platform technologies for spaceborne remote sensing*, vol. 5659, pp. 73–81, International Society for Optics and Photonics, 2005.
- Hansen, J., Sato, M., Kharecha, P., and Schuckmann, K. v.: Earth's energy imbalance and implications, *Atmospheric Chemistry and Physics*, 11, 13 421–13 449, 2011.
- Houghton, R.: Balancing the Global Carbon Budget, *Annual Review of Earth and Planetary Sciences*, 35, 313–347, <https://doi.org/10.1146/annurev.earth.35.031306.140057>, 2007.
- 10 Houweling, S., Breon, F.-M., Aben, I., Rödenbeck, C., Gloor, M., Heimann, M., and Ciais, P.: Inverse modeling of CO<sub>2</sub> sources and sinks using satellite data: a synthetic inter-comparison of measurement techniques and their performance as a function of space and time, *Atmospheric Chemistry and Physics*, 4, 523–538, 2004.
- Hungershofer, K., Breon, F.-M., Peylin, P., Chevallier, F., Rayner, P., Klonecki, A., Houweling, S., and Marshall, J.: Evaluation of various observing systems for the global monitoring of CO<sub>2</sub> surface fluxes, *Atmospheric chemistry and physics*, 10, 10 503–10 520, 2010.
- 15 Idso, C. D., Idso, S. B., and Balling Jr, R. C.: The relationship between near-surface air temperature over land and the annual amplitude of the atmosphere's seasonal CO<sub>2</sub> cycle, *Environmental and Experimental Botany*, 41, 31–37, 1999.
- Inoue, M., Morino, I., Uchino, O., Miyamoto, Y., Yoshida, Y., Yokota, T., Machida, T., Sawa, Y., Matsueda, H., Sweeney, C., et al.: Validation of XCO<sub>2</sub> derived from SWIR spectra of GOSAT TANSO-FTS with aircraft measurement data, *Atmospheric Chemistry and Physics*, 13, 9771–9788, 2013.
- 20 Jing, Y., Wang, T., Zhang, P., Chen, L., Xu, N., and Ma, Y.: Global Atmospheric CO<sub>2</sub> Concentrations Simulated by GEOS-Chem: Comparison with GOSAT, Carbon Tracker and Ground-Based Measurements, *Atmosphere*, 9, 175, 2018.
- Jones, C. D., Collins, M., Cox, P. M., and Spall, S. A.: The carbon cycle response to ENSO: A coupled climate–carbon cycle model study, *Journal of Climate*, 14, 4113–4129, 2001.
- Keppel-Aleks, G., Wennberg, P., and Schneider, T.: Sources of variations in total column carbon dioxide, *Atmospheric Chemistry and Physics*, 25 11, 3581–3593, 2011.
- Keppel-Aleks, G., Wennberg, P., Washenfelder, R., Wunch, D., Schneider, T., Toon, G., Andres, R. J., Blavier, J., Connor, B., Davis, K., et al.: The imprint of surface fluxes and transport on variations in total column carbon dioxide, *Biogeosciences*, 9, 875–891, 2012.
- Kong, S., Lu, B., Han, B., Bai, Z., Xu, Z., You, Y., Jin, L., Guo, X., and Wang, R.: Seasonal variation analysis of atmospheric CH<sub>4</sub>, N<sub>2</sub>O and CO<sub>2</sub> in Tianjin offshore area, *Science China earth sciences*, 53, 1205–1215, 2010.
- 30 Krishnapriya, M., Chandra, A. B., Nayak, K. R., Patel, N. R., Rao, P., and Dadhwal, V.: Seasonal and inter-annual variability of atmosphere CO<sub>2</sub> based on NOAA Carbon Tracker analysis and satellite observations, *Journal of the Indian Society of Remote Sensing*, pp. 1–12, 2017.
- Krol, M., Houweling, S., Bregman, B., Broek, M., Segers, A., Velthoven, P. v., Peters, W., Dentener, F., and Bergamaschi, P.: The two-way nested global chemistry-transport zoom model TM5: algorithm and applications, *Atmospheric Chemistry and Physics*, 5, 417–432, 2005.
- 35 Kulawik, S., Wunch, D., O'Dell, C., Frankenberg, C., Reuter, M., Oda, T., Chevallier, F., Sherlock, V., Buchwitz, M., Osterman, G., et al.: Consistent evaluation of GOSAT, SCIAMACHY, CarbonTracker, and MACC through comparisons to TCCON, *Atmospheric Measurement Techniques Discussions (Online)*, 8, 2015.

- Kulawik, S., Wunch, D., O'Dell, C., Frankenberg, C., Reuter, M., Oda, T., Chevallier, F., Sherlock, V., Buchwitz, M., Osterman, G., et al.: Consistent evaluation of ACOS-GOSAT, BESD-SCIAMACHY, CarbonTracker, and MACC through comparisons to TCCON, Atmospheric Measurement Techniques, 9, 683–709, 2016.
- Kuze, A., Suto, H., Nakajima, M., and Hamazaki, T.: Thermal and near infrared sensor for carbon observation Fourier-transform spectrometer on the Greenhouse Gases Observing Satellite for greenhouse gases monitoring, Applied optics, 48, 6716–6733, 2009.
- 5    Lei, L., Guan, X., Zeng, Z., Zhang, B., Ru, F., and Bu, R.: A comparison of atmospheric CO<sub>2</sub> concentration GOSAT-based observations and model simulations, Science China. Earth Sciences, 57, 1393, 2014.
- Liang, A., Gong, W., Han, G., and Xiang, C.: Comparison of Satellite-Observed XCO<sub>2</sub> from GOSAT, OCO-2, and Ground-Based TCCON, Remote Sensing, 9, 1033, 2017.
- 10   Lindqvist, H., O'Dell, C., Basu, S., Boesch, H., Chevallier, F., Deutscher, N., Feng, L., Fisher, B., Hase, F., Inoue, M., et al.: Does GOSAT capture the true seasonal cycle of carbon dioxide?, 2015.
- Liu, L., Zhou, L., Zhang, X., Wen, M., Zhang, F., Yao, B., and Fang, S.: The characteristics of atmospheric CO<sub>2</sub> concentration variation of four national background stations in China, Science in China Series D: Earth Sciences, 52, 1857–1863, 2009.
- Mengistu Tsidu, G.: High-resolution monthly rainfall database for Ethiopia: Homogenization, reconstruction, and gridding, Journal of Climate, 25, 8422–8443, 2012.
- 15   Mengistu Tsidu, G., Blumenstock, T., and Hase, F.: Observations of precipitable water vapour over complex topography of Ethiopia from ground-based GPS, FTIR, radiosonde and ERA-Interim reanalysis, Atmospheric Measurement Techniques, 8, 3277, 2015.
- Mitchell, T.: Africa Rainfall Climatology. University of Washington, 2001.
- Morino, I., Uchino, O., Inoue, M., Yoshida, Y., Yokota, T., Wennberg, P., Toon, G., Wunch, D., Roehl, C., Notholt, J., et al.: Preliminary validation of column-averaged volume mixing ratios of carbon dioxide and methane retrieved from GOSAT short-wavelength infrared spectra, 2010.
- 20   Nagarajan, B. and Aiyyer, A. R.: Performance of the ECMWF operational analyses over the tropical Indian Ocean, Monthly weather review, 132, 2275–2282, 2004.
- Nayak, R., Deepthi, E., Dadhwal, V., Rao, K., and Dutt, C.: Evaluation of NOAA Carbon Tracker Global Carbon Dioxide Products, The International Archives of Photogrammetry, Remote Sensing and Spatial Information Sciences, 40, 287, 2014.
- 25   NIES GOSAT Project, .: Summary of the GOSAT Level 2 data Products Validation Activity, Center for Global Environmental Research, pp. 1–10, 2012.
- O'Dell, C., Connor, B., Bösch, H., O'Brien, D., Frankenberg, C., Castano, R., Christi, M., Eldering, A., Fisher, B., Gunson, M., et al.: The ACOS CO<sub>2</sub> retrieval algorithm-Part 1: Description and validation against synthetic observations, 2012.
- 30   Olsen, S. C. and Randerson, J. T.: Differences between surface and column atmospheric CO<sub>2</sub> and implications for carbon cycle research, Journal of Geophysical Research: Atmospheres, 109, 2004.
- Patra, P. K., Crisp, D., Kaiser, J. W., Wunch, D., Saeki, T., Ichii, K., Sekiya, T., Wennberg, P. O., Feist, D. G., Pollard, D. F., et al.: The Orbiting Carbon Observatory (OCO-2) tracks 2–3 peta-gram increase in carbon release to the atmosphere during the 2014–2016 El Niño, Scientific reports, 7, 13 567, 2017.
- 35   Peters, W., Jacobson, A. R., Sweeney, C., Andrews, A. E., Conway, T. J., Masarie, K., Miller, J. B., Bruhwiler, L. M., Pétron, G., Hirsch, A. I., et al.: An atmospheric perspective on North American carbon dioxide exchange: CarbonTracker, Proceedings of the National Academy of Sciences, 104, 18 925–18 930, 2007.

- Raupach, M. R., Marland, G., Ciais, P., Le Quééré, C., Canadell, J. G., Klepper, G., and Field, C. B.: Global and regional drivers of accelerating CO<sub>2</sub> emissions, *Proceedings of the National Academy of Sciences*, 104, 10288–10293, 2007.
- Rayner, P. and O'Brien, D.: The utility of remotely sensed CO<sub>2</sub> concentration data in surface source inversions, *Geophysical research letters*, 28, 175–178, 2001.
- 5 Rodgers, C. D. and Connor, B. J.: Intercomparison of remote sounding instruments, *Journal of Geophysical Research: Atmospheres*, 108, 2003.
- Saitoh, N., Imasu, R., Ota, Y., and Niwa, Y.: CO<sub>2</sub> retrieval algorithm for the thermal infrared spectra of the Greenhouse Gases Observing Satellite: Potential of retrieving CO<sub>2</sub> vertical profile from high-resolution FTS sensor, *Journal of Geophysical Research: Atmospheres*, 114, 2009.
- 10 Santer, B. D., Painter, J. F., Bonfils, C., Mears, C. A., Solomon, S., Wigley, T. M., Gleckler, P. J., Schmidt, G. A., Doutriaux, C., Gillett, N. P., et al.: Human and natural influences on the changing thermal structure of the atmosphere, *Proceedings of the National Academy of Sciences*, 110, 17235–17240, 2013.
- Stocker, B. D., Roth, R., Joos, F., Spahni, R., Steinacher, M., Zaehle, S., Bouwman, L., Prentice, I. C., et al.: Multiple greenhouse-gas feedbacks from the land biosphere under future climate change scenarios, *Nature Climate Change*, 3, 666–672, 2013.
- 15 Stocker, T.: *Climate change 2013: the physical science basis: Working Group I contribution to the Fifth assessment report of the Intergovernmental Panel on Climate Change*, Cambridge University Press, 2014.
- Tsutsumi, Y., Mori, K., Hirahara, T., Ikegami, M., and Conway, T. J.: Technical report of global analysis method for major greenhouse gases by the World Data Center for Greenhouse Gases, World Meteorological Organization, 2009.
- Wilks, D. S.: *Statistical methods in the atmospheric sciences*, vol. 100, Academic press, 2011.
- 20 Williams, C. A., Hanan, N. P., Neff, J. C., Scholes, R. J., Berry, J. A., Denning, A. S., and Baker, D. F.: Africa and the global carbon cycle, *Carbon balance and management*, 2, 3, 2007.
- Wunch, D., Wennberg, P., Toon, G., Connor, B., Fisher, B., Osterman, G., Frankenberg, C., Mandrake, L., O'Dell, C., Ahonen, P., et al.: A method for evaluating bias in global measurements of CO<sub>2</sub> total columns from space, *Atmospheric Chemistry and Physics*, 11, 12317–12337, 2011.
- 25 Yokota, T., Yoshida, Y., Eguchi, N., Ota, Y., Tanaka, T., Watanabe, H., and Maksyutov, S.: Global concentrations of CO<sub>2</sub> and CH<sub>4</sub> retrieved from GOSAT: First preliminary results, *Sola*, 5, 160–163, 2009.
- Yokota, Y., Matsunaga, T., Ohtake, M., Haruyama, J., Nakamura, R., Yamamoto, S., Ogawa, Y., Morota, T., Honda, C., Saiki, K., et al.: Lunar photometric properties at wavelengths 0.5–1.6  $\mu\text{m}$  acquired by SELENE Spectral Profiler and their dependency on local albedo and latitudinal zones, *Icarus*, 215, 639–660, 2011.
- 30 Yoshida, Y., Kikuchi, N., Morino, I., Uchino, O., Oshchepkov, S., Bril, A., Saeki, T., Schutgens, N., Toon, G., Wunch, D., et al.: Improvement of the retrieval algorithm for GOSAT SWIR XCO<sub>2</sub> and XCH<sub>4</sub> and their validation using TCCON data, 2013.
- Zhou, T., Yi, C., Bakwin, P. S., and Zhu, L.: Links between global CO<sub>2</sub> variability and climate anomalies of biomes, *Science in China Series D: Earth Sciences*, 51, 740–747, 2008.